AntBot: a six-legged walking robot able to home like desert ants in outdoor environments

Julien Dupeyroux, Julien Serres, Stéphane Viollet

Title

- Full title:

  AntBot: a six-legged walking robot able to home like desert ants in outdoor environments

- Short title:

  A walking robot homing like desert ants

Authors

Julien Dupeyroux,[1] Julien R Serres,[1] Stéphane Viollet[1*]

Affiliations

[1] Aix Marseille Univ, CNRS, ISM, Marseille, France

[*] Corresponding author. Email: stephane.viollet@univ-amu.fr

Abstract

Autonomous outdoor navigation requires reliable multi-sensory fusion strategies. Desert ants travel widely every day showing unrivalled navigation performances, using only a few thousand neurons. In the desert, pheromones are instantly destroyed by the extreme heat. To navigate safely in this hostile environment, desert ants assess their heading from the polarized pattern of the skylight and judge the distance travelled based on both a stride-counting method and the optic flow, i.e., the rate at which the ground move across the eye. This process is called the path integration (PI). Although many methods of endowing mobile robots with means of outdoor localization have been developed recently, most of them are still prone to considerable drift and uncertainty. Here it was proposed to test several ant-inspired solutions to outdoor homing navigation problems on a legged robot using two optical sensors equipped with just 14 pixels, two of which were dedicated to an insect-inspired compass sensitive to ultraviolet light. When combining with two rotating polarized filters, this compass was equivalent to two costly arrays composed of 374 photosensors, each of which tuned to a specific polarization angle. The other 12 pixels were dedicated to optic flow measurements. Results show that our ant-inspired methods of navigation give precise performances: the mean homing error recorded during the overall trajectory was as small as 0.67% under similar lighting conditions to those encountered by ants. These findings show that ant-inspired PI strategies can be used to complement classical techniques with a high level of robustness and efficiency.

Summary

Our ant-inspired robot returned home outdoor with a mean error of only 6.5cm after covering various distances (between 5m and 14m).

Introduction

To keep up with the fast development of fully autonomous mobile robots, there is an urgent need to design navigation systems with a high level of reliability, repeatability and robustness. The potential applications of these robots are many and various: they can be used for exploring unknown places, for instance, after natural disasters or in extra-terrestrial environments where both wireless communications and GPS transmission can overcome signal failures; for inspecting urban infrastructures; for the long-range transportation of people and goods; for automatic crop inspection and harvesting; for

autonomous marine navigation (container ships); and for performing reconnaissance missions.

Nowadays, the civilian global positioning system (GPS) is the main method used for obtaining the information required to determine a position on Earth. GPS is now integrated into many connected devices such as smartphones, watches, and cars, but it is accurate within a range of only up to 4.9m on smartphones, and even less near urban infrastructures, canyons and trees (*1*). Vision-based systems are the second most frequently used means of specifying the position of mobile systems. Simultaneous localization and mapping (SLAM) methods are widely used these days in autonomous cars, planetary rovers, and unmanned aerial vehicles (UAVs), for instance, working both indoors and outdoors (*2–4*). Depending on the environment for which they are designed, SLAM algorithms can reach high levels of precision although the computing costs are extremely high. In addition, the performances of vision-based methods depend strongly on the presence of consistent brightness, which seldom occurs in outdoor situations (*5*, *6*). Event-based cameras are another possible way of solving vision-based localization problems, again using SLAM algorithms, as recently done with a dynamic vision camera (DVS or DAVIS camera) performing visual odometry (*7*). Laser detection and ranging methods, i.e. LIDAR-based methods, also provide high-resolution maps which can be used in autonomous cars and robots (*8*). Unfortunately, the excellent performances obtained with all these methods can be achieved only at a high price in terms of the physical overload and the high computational cost. The latter technique makes use of proprioceptive-based approaches, mostly involving inertial measurement units (IMUs), in which accelerometers are combined with rate gyros and magnetometers. These devices can be combined with GPS to improve the overall accuracy (*9*). Although a wide range of commercial IMUs are available, these sensors are still subject to long-term drift in both the static and dynamic modes, as well as being highly sensitive to the electromagnetic interferences generated by ferrous building components.

To summarize, it would be of great interest to take advantage of all advanced navigation techniques to set up a new powerful, reliable, robust navigation system. The aim of this paper is therefore to present a novel navigation system inspired by desert ants' navigation behavior, which requires precise and robust sensory modalities.

Homing without GPS: an ant-based approach

Desert ants are known to be highly efficient navigators as they can find their way back home after foraging for hundreds of meters in hostile environments (Fig. 1A) (*10*). Here we proposed to take our inspiration from desert ants by developing a hexapod walking robot based on insect-inspired navigation models developed from the mid-70s to the late 90s. This robot called AntBot, which is equipped with minimalistic bio-inspired sensors, was tested under outdoor conditions in a series of homing tasks. In line with previous bio-inspired studies (*11*, *12*), we adopted a dual objective. First, we seek to provide biologists who have developed ant-based behavioral models with a robotic platform which can be used to obtain field results in the same environments as insects. Then we aim to provide roboticists with new robust autonomous navigation strategies which can be implemented outdoors. This strategy could be combined with other traditional techniques to improve the localization performances and to decrease the risks involved in navigating in GPS-denied environments.

Desert ants' navigation systems differ greatly from those of other ant species. Classically, ants locate their nest by retracing the pheromone trails they have created during their foraging trip. In the desert, the heat of the ground destroys these pheromone trails. Desert ants therefore use proprioceptive and visual cues to find their way (*10*, *13*). To navigate between their nest and food places, desert ants such as *Cataglyphis fortis* and *Melophorus bagoti* use a combination of several modes: the path integration (PI) mode, which involves only a few cues including the number of strides, the ventral optic flow (OF) cues based on the slip speed of the ground over the retina, the celestial-based orientation cues; and visual guidance (VG) processes in cluttered environments containing prominent landmarks, which consists in memorizing and comparing snapshots (for a review of behavioral studies and models and studies on VG (*14–17*). For several decades, experiments have been conducted on desert ants with a view to understanding how PI works (*18–21*) and how ants choose between PI and VG. It has been observed that foraging ants always update their PI processes (*14*), even when applying VG. Under several circumstances, ants have been found to use a weighted combination of PI and VG routines (*22*). Ants were also found to mostly rely on PI when the visual scenery was less familiar (*23*). PI in desert ants can be said to resemble an Ariadne's thread or a proxy strategy which is never switched off, the precision of which is not necessarily improved when the trajectory is repeated (*10, 24*).

Celestial cues, including both the pattern of polarization of the skylight and the sun's elevation, are widely used among desert ants (*25–28*). Previous studies have shown that the insects' compound eye contains a small region called the dorsal rim area (DRA), where the photoreceptors are sensitive to polarized light (*29*). As the pattern of polarized skylight is largely symmetric about the solar meridian, it provides a reliable orientation cue for long-distance navigation since it can be used to estimate the heading angle (*30*). It has been reported that most species show maximum sensitivity in the ultraviolet (UV) range (*31*). Although many suggestions have been put forward to explain the predominance of UV cues, the main reason may lie in the persistence of the UV light through the clouds and canopies (*32*). The insects' celestial compass therefore remains stable even when clouds are crossing the sky, which enables them to update their PI seamlessly with orientation information. However, the polarized pattern of skylight is determined by the position of the sun in the sky, the movement of which results in the gradual translation of the angle of polarization (AoP). If this shift was not compensated for, it would cause detrimental drift in the insect's PI. Ants can integrate the solar ephemeris templates in line with the circadian clock and thus correct the estimated heading angle (*33–36*).

A model for the polarization neurons (POL-neurons) based on studies on the DRA of crickets was presented by Labhart (*37*). In the optic lobe, the POL-neurons' activity is a sinusoidal function of the polarization orientation, *i.e.* an e-vector. The latter author also established that POL-neurons' responses include three preferential angles of polarization, 10°, 60° and 130°, with respect to the body's longitudinal axis. The DRA ommatidia are known to be simultaneously sensitive to one e-vector and its corresponding orthogonal. In the model proposed by Labhart, an e-vector can be calculated from the log-ratio between the two photoreceptors' responses, that based on one e-vector, and that based on the orthogonal e-vector. This is precisely the model we have implemented on board our hexapod robot.

Background and related studies in the field of robotics

The first robotic implementation of the desert ants' DRA was presented in (*38*). In this robot, the sensor was composed of three pairs of polarization-sensitive units (POL-units) with a spectral sensitivity in the visible range. Each POL-unit was composed of two photodiodes topped with linear polarizing filters set orthogonally to each other to mimic the photoreceptors present in the DRA. The POL-units were aligned according to three different orientations (0°, 60° and 120°). The polarization model described by Labhart was implemented and the mean error recorded was found to be equal to 0.66° (*37*). Chu *et al.* developed a smaller compass consisting of 6 photodiodes topped with linear polarizers 60° apart from each other (*39*). The spectral sensitivity of the compass was in the blue range (400—520nm) and the data processing method used was the same as that described in (*40*). Experiments in a controlled environment yielded a mean error of ±0.2°. A polarization dependent photodetector based on a bilayer nanowire was recently developed and tested under artificial blue lighting, giving a mean error of only ±0.1° once a polynomial fitting process had been applied (*41*). Other implementations of wire grid micro-polarizers have been developed, some of which involved different AoPs (involving regular shifts of 45°) (*42*). Another biomimetic celestial compass was presented by Chahl & Mizutani in (*43*). The polarization sensor was composed of three pairs of photodiodes topped with linear polarizers as in (*40*) and used concomitantly with a bio-inspired version of the insects' ocelli (*44*). Bio-inspired approaches have also been adopted with cameras in the visible range (*45*) along with the polarization model developed in (*40*). Concurrently with the biomimetic approach, other authors have developed polarization sensors in line with the physical theory of skylight polarization by computing the Stokes' parameters to determine the degree of linear and circular polarization (DoLP and DoCP, respectively) and the AoP (*46–48*).

Although various bio-inspired celestial compasses have been implemented in the field of robotics, few robots have been developed so far which are able to perform ant-inspired autonomous robotic navigation tasks. In the late 1990s, the Sahabot 1 and 2 wheeled robots were pioneers in this field as they were able for the very first time to perform outdoor homing navigation tasks based on ant-inspired sensors and navigation models (PI and VG), with outstanding results. Relying on PI processes alone, Sahabot 2 gave a mean error of 13.5cm (in the case of a 70-m long trajectory) with a standard deviation of 6.3cm (*40*) under optimal lighting conditions. To achieve this high level of performance, an improved version of the celestial compass embedded on-board Sahabot 1 (*38*) was used in the visible range to compute the robot's heading. The problem of solar ambiguity was solved by using additional photodiodes to detect the location of the sun in the sky. The robot computed the distance travelled by integrating information provided by wheel encoders. Chu et al. also recently embedded their first celestial compass on-board a 2-wheeled robot and obtained a mean homing error of 42cm in the case of a 32-m long trajectory (*49*).

Bio-inspired odometry: counting or not counting?

In all the robotic tests described above, odometry was performed using wheel encoders. Many hypotheses have been put forward to explain how insects measure the distance travelled (odometry) when foraging in unknown environments. Flying insects are thought to mostly use OF cues (*50*) and snapshot images (*51*). *Cataglyphis* and *Melophorus* desert ants can collect distance information from multiple sources: the panoramic OF or snapshot images (*20*, *52*, *53*), the panoramic skyline (*54*), ventral OF (*55*), and stride integration methods, which have been called the insects' pedometer (*56–58*). Panoramic vision-based methods seem to be mostly applied when navigating in cluttered environments, where the

obstacles detected can be used by insects as landmarks to find the location of the goal. Unfortunately, this method does not explain the straight-ahead homing paths adopted by walking insects at the end of their very first exploration of a new food source (Fig. 1A). Foragers' PI odometer is now known to rely mainly on proprioceptive cues (stride integration methods), but also, in some specific cases, to combine these methods with visual information (ventral OF) in order to constantly track the distance to both the nest and food areas (*59*). Other studies have suggested that both odometric cues (OF or stride counting methods) are acquired during the foraging trip and can then be used, independently or not, to regain the nest entrance (*60*). These PI cues can also be combined with VG to increase the accuracy and the robustness of the homing procedure when foragers are crossing regions of interest they have previously explored (*24*).

Contributions

Autonomous navigation was successfully performed here with a legged robot endowed with two insect-inspired optical sensors comprising only 14 pixels in overall, two of which were dedicated to a compass sensitive to UV light. When combining this pair with two rotating polarized filters, this compass was equivalent to two arrays composed of 374 pixels, each of which tuned to a specific polarization angle. The other 12 pixels were dedicated to optic flow measurements and were able to adapt autonomously to large changes in light intensity. In addition, the data fusion method presented here mimics a highly precise, robust dead reckoning strategy. These advances, in addition to recent findings on walking recovery in legged robots which have been damaged during the foraging trip (*61*), open up many possibilities for legged robots in the field of real-world navigation.

In this study, the robot was set several homing tasks using various sensory modes such as internal knowledge of its stride integration processes, the use of the ventral OF, and that of celestial-based orientation (Fig. 1B). Five PI modes were therefore designed and implemented in order to determine the homing trajectory in the same way as desert ants. The performances and the reliability of these modes were determined on the basis of 130 trajectories. Successful homing trajectories were taken to be those in which the robot ended up in a homing area defined as a circular area around the departure point, the radius of which was equal to half of the robot's diameter (22.5cm).

We show that our autonomous robot's performances are robust to weather conditions and UV-index changes. In addition, our ant-inspired navigation strategy can be applied to any mobile system evolving in open air environments (cars, ships, drones, wheeled robots). In the long run, we believe that autonomous walking robots will be reliable enough to explore rough terrains in GPS and communication denied environments where our ant-inspired navigation strategy could be used as a genuine navigation system.

Results

Five different ant-inspired homing methods were therefore designed and tested here in order to gradually add sensory information about the heading and the odometry to our hexapod robot AntBot until the desert ants' PI was completely mimicked, and then select the best model for use in low-computational, high efficiency, robust navigation.

Designing a robotic ant

AntBot is a hexapod robot equipped with insect-inspired optical sensors and driven by ant-inspired navigational models to be tested under real-life conditions (Figs. 2ACD and S1). It has three degrees of freedom per leg and is fully 3-D printed. The walking gait of the AntBot robot was directly inspired by ants' highly regular tripod gait (*62*, *63*). The walking gait obeys a fixed pre-programmed pattern. It is worth noting, however, that real insects' walking behavior is slightly different from that implemented in AntBot. Chronographs of the walking patterns of *Cataglyphis bicolor* desert ants (Fig. S1D) have shown that ants' legs show different transfer and pause times: the midlegs' transfer times are shorter than those of the other legs. In addition, the transfer phase starts at different times between the front and hind legs. AntBot's gait is far more regular, since it shows steady synchronous transfer and pause times and departure times (Fig. S1E). The robot's walking pattern is determined entirely by just a few parameters, which are directly adjustable via the terminal command. These parameters are described in Table S1, which also gives the values used in this study. AntBot's walking performances were tested in the Flight Arena of the Mediterranean (a 6-m wide, 8-m long, 6-m high arena) equipped with 17 motion-capture cameras. Its straight forward walking pattern was determined in terms of the mean walking stride length (8.2cm) and the mean turning angle per turning stride (10.9°), based on the parameters of interest in this study. AntBot is equipped with multiple minimalistic sensors mimicking the desert ants' navigational toolkit: an insect-inspired celestial compass (*64*, *65*) and a bio-inspired OF sensor called M²APix (*66*, *67*). Details of the robot's electronic architecture and its structure are presented in Fig. 2B. All the sensors and electronic parts are controlled by an embedded micro-computer (Raspberry Pi2B board) dedicated to sensor data acquisition, data processing, and navigation. The robot weighs 2.3kg including its batteries. It can reach a maximum speed of approximately 90cm/s and has a maximum autonomy of 30 minutes.

The estimated heading angle is determined on-board on the basis of the celestial pattern of polarization described in Fig. 3A. Because of the Rayleigh scattering of sunlight, interactions between the photons and the constituents of the Earth's atmosphere produce a regular pattern across the sky (*68*, *69*). Along the solar and anti-solar meridians, the AoP is known to be perpendicular to the meridians. We made use of this property in our novel ant-inspired celestial compass (Fig. 3BC and S2) (*64*). The compass is composed of two polarization units (POL-units) consisting of two UV light sensors (Sg01D18, *SgLux*) topped with actuated rotating linear sheet polarizers. The angular aperture of each POL-unit is about 120° (Fig. S3) and the angular resolution is arbitrarily set at 0.96°, with an acquisition period of approximately 20 seconds due to the full rotation of the polarizers. This time multiplexing solution, though not existing in the DRA of insects, is an engineering solution that reproduces the full DRA with minimal overload for the robot by generating 2×374 measurements in an acquisition period. According to the model for POL-neurons found to exist in crickets by Labhart (*37*), this celestial compass determines the AoP by analyzing the log-ratio between the two POL-units' signals (Fig. 3DE; for further details, see Text S1). Preliminary tests on the previous version of AntBot called Hexabot showed that this sensor is highly reliable and suitable for performing navigation tasks in various meteorological contexts (high/low UV indexes, clear/overcast sky) (*64*). The statistical performances of the celestial compass were tested under various meteorological conditions (Figs. S4, S5, and S6).

Our celestial compass is sensitive to changes in the sky and the changing effects of clouds on the AoP. Previous results showed that even with a signal acquisition time as long as 20 seconds, the robot was still able to determine its heading angle with great precision: the median error was 0.02° when the sky was slightly cloudy, and 0.59° in the case of an

overcast sky (*65*). To solve the ambiguity between the solar and anti-solar heading angles, AntBot was made to roll its celestial compass to the left and right to detect the part of the sky containing the sun (Fig. S7). This approach is fairly in line with recent findings on the locust's brain: polarization-specific neurons are activated in response to direct sunlight, which has been taken to possibly explain how the solar ambiguity may be solved in the insect's brain (*36*, *70*).

As observed in desert ants, distance information can be obtained by using either ventral OF measurements or stride integration methods. AntBot is equipped with a 12-pixel OF sensor called M²APix (Michaelis-Menten Auto-adaptive Pixels, Fig. 4AB) mounted facing the ground. The M²APix measures the OF at a high rate and shows auto-adaptability to light changes within a 7-decade range (*66*). This sensor was characterized, and its inter-pixel angle $\Delta\varphi$ was found to be equal to 3.57° with a standard deviation of 0.027° (Fig. S8). Its signal to noise ratio (SNR) was also measured, giving a mean value of 32dB. The sensor is composed of two rows of six hexagonal pixels (Fig. 4C). Two adjacent pixels, which are referred to here as a LMS (a Local Motion Sensor), are used to determine the time lag between two adjacent pixels' detection of the same moving edge (Fig. 4D). The OF is equal to the ratio between the inter-receptor angle and this time lag. To compute a precise and reliable OF value, the time lags of all the LMSs were compared with a threshold defined by the robot's average speed (Fig. 4E). The final OF value was calculated using only the time lags that were not rejected by the threshold process. The height variation of the robot's center of mass while walking amounts to less than 1cm in comparison with the height of the sensor (approximately 22cm) and can therefore be taken to have no effect on the average OF value. The distance travelled can therefore be computed based on OF measurements while the robot is walking straight ahead (Text S2).

Experimental context

These experiments were performed in Marseille, in the South of France, in front of our laboratory (43°14'02.1" N, 5°26'37.4" E) from January 5 to February 16, 2018. This place is surrounded by mountains, but the sun remained visible all day long. The meteorological conditions were stable, with little wind and a clear sky (French meteorological services) (Fig. S9). According to the European Space Agency, the UV-index generally ranged around 1.0, showing little variability (< 20%) in early January, and reached 1.6 in mid-February, when the last experiments were performed. All the experiments not requiring the celestial compass were performed indoors in the Flight Arena of the Mediterranean. To ensure that neither the walking performances of AntBot nor the OF-based odometric cues would bias the homing results, flat textured panels were used in all the experimental set-ups (Fig. S10).

The dynamic behavior of AntBot's servos is highly dependent on the ambient temperature, as the servos tend to heat up after long periods of use, resulting in locomotor failure. Because of this limitation, the servos' temperature had to be strictly monitored when the experiments were conducted during the afternoon (when the temperatures ranged from 10°C to 18°C). It was observed during previous tests that the average distance walked tends to differ between morning and afternoon conditions. This can be explained by the great difference in temperature, ranging from -2°C to 8°C in the morning to more than 10°C in the afternoon. An ad-hoc correction was therefore applied to the robot's navigation modes (Table S2). Lastly, the robot was powered by an external power supply during all the experiments to make them easier to perform and to ensure that the robot's dynamics would remain steady during all the navigation tasks.

Ant-inspired path integration models

As desert ants can retrieve navigation cues using stride integration, ventral OF and skylight polarization processes, the following five PI modes were implemented:

(a) A PI-ST mode (a blind mode), where both the distance and the computed orientation were based solely on the stride integration process. The stride integration was performed using a motor control signal sent to the robot's controller.

(b) A PI-OF-ST mode based on the ventral OF odometry and the stride-based estimation of the heading angle.

(c) A PI-ST-FUSE mode based on a stride-based estimate of the robot's heading angle and a combination between the stride integration and the ventral OF cues to determine the distance travelled.

(d) A PI-POL-ST mode based on the polarization of the skylight to determine the heading angle, and a stride count to estimate the distance.

(e) The fully ant-inspired PI-Full mode based on the celestial compass to estimate the heading angle, and a custom-made combination between the stride integration method and the ventral OF to determine the distance travelled (Text S2 and Table S2).

The path integrator is outlined in Text S3 regardless of the sensory modes involved.

Navigation experiments

The outdoor experiments were conducted as follows: the foraging trajectory included N checkpoints (Fig. S11); the homing phase was divided into N_H checkpoints, thus enabling the robot to exactly measure and correct its own drift when using its celestial and OF sensors. The robot stopped at each checkpoint in order to determine the AoP before performing the next navigation segment. To test the five PI modes of interest here, 3 series of experiments were performed. In the first series, a 5-checkpoint trajectory was tested and repeated 20 times in each PI mode. The overall foraging trip was about 5-m long and involved a 2-m long homing trajectory. In the second series of experiments, five random 5-checkpoint trajectories were tested with greatly varying distances. Lastly, a 10-checkpoint trajectory corresponding to an overall distance of 14m was tested.

The first random 7-m long trajectory was tested and repeated 20 times in order to check the repeatability of the robot's homing performances (Fig. 5). The greatest median error was reached with the PI-ST mode (error: 7.29%), showing a high level of variability (Fig. 5A), while the lowest median error was recorded with the PI-Full mode (Fig. 5E): in this case, the error was 0.97% and the minimum error recorded was equal to 0.17%. Some of the experiments were conducted under changeable sky conditions, but the results were combined with those obtained under a clear sky as there were no significant differences in the corresponding homing performances (all the experiments conducted under a changeable sky led to homing success). It can be observed that the greatest variability among the homing locations corresponded to the PI-OF-ST mode (Fig.5B), as the confidence ellipse had the largest area (2638cm²) in this case, but the homing trajectories were more home-directed with this mode than in the PI-ST tests. Non-celestial methods (Fig. 5B) and (Fig. 5C) gave poor homing performances, as less than 25% of the 20 experiments resulted in homing success, but the use of the ventral OF improved the results (Fig. 5BC) in terms of the size of the ellipse. With the PI-POL-ST mode, the orientation estimate obtained was correct as AntBot's homing path was oriented towards the goal, and

the homing location was nearer to the goal and showed less variability, as the confidence ellipse measured only 1409cm² in this case (Fig. 5D). The orientation of the confidence ellipse shows that the homing distance was variable: the major axis was oriented in the homing direction and the center of the ellipse was located near the goal, which means that some of the distances in these experiments were either under- or overestimated. The confidence ellipse of the homing locations in the PI-Full mode (Fig. 5E) had the smallest area (236cm², i.e. 10% of the largest area) and tended to have a circular shape. Lastly, the violin plots of the homing error show that the density probability had a normal distribution with the PI-ST, PI-OF-ST, and PI-Full modes (Lilliefors normality tests, p-value > 0.05) (Fig. 5ABE).

We then investigated the influence of the length and shape of the trajectory on the homing performances: 5 random trajectories were generated and tested with various shapes and distances (from 4.7m to 10.2m) (Fig. 6). The PI-ST mode gave a mean error equal to 9.37% of the entire journey, but the largest error was obtained with the PI-OF-ST mode, which gave a mean error of 11.58%. The PI-POL-ST mode resulted in a mean error of 2.99% and a low level of variability (*sd*: 1.3%). Once again, the full sensor and the ant-like PI-Full mode resulted in the lowest mean error (0.65%) and a low standard deviation (*sd*: 0.28%). Comparisons between the results of these experiments and those obtained in the first series clearly showed that the shape of the trajectory did not affect the robot's homing performances. The violin plots obtained were similar to the previous ones presented in Fig. 5. The normal distribution of the homing distance error was also established in the case of all the PI modes tested (Lilliefors normality tests, p-value > 0.05).

However, the lengths of the trajectories tested here (Fig. 6) differed considerably (by up to 1.5m), which may explain the variations in the homing performances observed in comparison with those presented in Fig. 5. We therefore conducted a third series of experiments in which AntBot was made to walk for more than 10m taking a random trajectory, and then return to its starting-point (giving a homing distance equal to approximately 4m). This long-distance trajectory was tested only once with each PI mode and recorded (Movies S1 – S5). The long-distance trajectories recorded are shown in Fig. 7. The greatest homing error was 13.44% (171.1cm in the PI-ST mode). The lowest homing error was recorded with the PI-Full mode, where the error was 6.47cm, corresponding to 0.47% of the entire trajectory (Figs. 1B and 7). The homing errors recorded with all the PI modes were similar to those obtained in the two previous series of experiments (two-tailed *t-test*: p-value > α_C where α_C = 0.05/5 using a Bonferroni correction procedure).

The overall results of the 26 experiments performed in all the PI modes are summarized in Tables S3 – S7. The ground truth data were compared with the results obtained with the robot using the PI method (Tables S3 – S7). The results showed that the robot's PI was nearest to the ground truth with the PI-Full mode, showing a root mean square error (RMSE) of the homing location between the ground truth and the robot's endpoint of 4.6cm (this value jumped to 65.0cm with the PI-ST mode). The homing errors, expressed as a percentage of the entire trajectory, are presented in Fig. 8B in the case of each PI mode, depending on the experiments. As expected in view of Figs. 5, 6 and 7, AntBot gave the lowest homing error with the PI-Full mode (one-tailed *t-test*: p-value > α_C where α_C = 0.05/5 using a Bonferroni correction procedure), corresponding to a mean error of 0.67% ± 0.27% (i.e., a mean error of 6.67cm ± 2.7 cm). These results show that the distance did not significantly affect the homing performance in the PI-Full mode: the

homing error in the case of the 14m-long trajectory was 6.47cm, which differed by only 3% from the mean values obtained in all the experiments. The criterion used to determine whether an experiment was a homing success or not was whether the robot's center of mass was located within a disk with a radius of 22.5cm (i.e., half of the robot's diameter) centered on the robot's starting-point. Fig. 8A gives the homing success rates achieved in the experiments depending on the homing criterion, ranging here between *L* and *L/16*, where *L* is the robot's diameter (45cm). Except for the PI-POL-ST and PI-Full modes, none of the PI modes gave homing success rates of more than 90% (with either homing criterion). The PI-POL-ST mode gave a homing success rate of 97% when the homing criterion was set at *L*, but this value dropped sharply to less than 60% at *L/2*. The PI-Full mode gave a 100% homing success rate with both homing criteria *L* and *L/2*. At *L/4* (i.e. 11.3cm), all the PI modes, except the PI-Full mode, yielded homing success rates below 10%, while that obtained with the PI-Full mode was still greater than 90%. This trend shows how accurate and repeatable the fully ant-inspired PI-Full mode is, although it requires only 2 pixels for celestial vision and 12 pixels for the ventral OF acquisition.

Discussion

Five ant-inspired PI modes were tested here on-board our hexapod robot AntBot. Most of the previous ant-based visual compasses were sensitive in the visible range, whereas AntBot was the first robot to be equipped with a DRA-inspired celestial compass which acquires the AoP in the UV-range, and with a ventral OF sensor composed of 12 auto-adaptive pixels. The PI-Full mode, in which celestial cues (skylight polarization and sun position cues) are used to estimate the heading angle, and ventral OF and stride integration processes are used to estimate the travel distance, resulted in highly accurate homing performance and a very low homing error of 0.67% ± 0.27% (Fig. 8), and few differences were observed between the ground truth and the robot's distance estimations (RMSE: 4.6cm) (Table S7). The results obtained here show that these performances did not depend on either the shape or the length of the trajectory, which means that the PI-Full mode is a highly suitable basis for autonomous navigation in open air environments. If it is combined with other reliable dead reckoning techniques (*70*), our results could considerably open the possibilities for legged robots to navigate in real environment, where wheeled robots are hampered by their own structure. However, the present results prove that heading information can also be reliably determined on the basis of purely odometric cues (stride-counting methods and OF-measurements), using the PI-OF-ST and PI-ST-FUSE modes. However, the robustness of the celestial compass under changeable weather condition has been clearly shown in (*65*) where the proposed *AntBot* method features greater performances than the *Sahabot* method.

Some of the experiments were conducted under changeable sky conditions. In all the outdoor experiments combined, the homing success rate recorded under a cloudy sky was equal to 100% with the *L/2* homing distance criterion (Fig. 8A, Tables S6 and S7). Future studies will focus on the large-scale repeatability of these results under changeable sky conditions.

Ant-inspired autonomous navigation methods have yielded good performances on wheeled robots (*40*, *49*). The lowest mean homing error was obtained with the Sahabot 2 robot, but the standard deviations were rather high in comparison with AntBot's present performances: Sahabot 2: 13.5cm ± 6.3cm in the case of a 70-m long trajectory (0.19%); Chu et al. (*49*): 42cm in that of a 32-m long trajectory (1.31%); versus AntBot: 6.47cm in the case of a 14-m long trajectory (0.46%). It is worth discussing the differences between

these wheeled robots and desert ants. (i) There obviously exist no morphological or locomotor similarities between rovers and ants or legged robots, and rovers have a significant advantage here, since wheeled machines are less prone to drift than their legged counterparts. Rovers can easily acquire celestial information, whereas desert ants collect their celestial cues with great precision despite heavy yaw, pitch and roll disturbances while they are travelling at high speed (*62*). Based on extensive studies carried out at our laboratory on attitude disturbances in our previous Hexabot robot (*71*), we can assume that AntBot, which is equipped with the same controller as Hexabot, faces the same attitude disturbances as desert ants when walking with tripod gait. Besides, AntBot can navigate in any kind of terrestrial environments, flat or rough, while wheeled robots are inherently limited to specific applications. (ii) The celestial compasses implemented in these studies were all designed to measure the polarized light in the visible range, whereas desert ants perceive their celestial cues in the UV range (*31, 32*), the principle of which is used in the celestial compass embedded on-board AntBot. The previous experiments were performed under clear sky conditions in the early morning or late afternoon to prevent the sensors from being saturated by the sun, whereas desert ants are known to forage during the hottest time of day, *i.e.* when the sun is near the zenith and the DoLP is at its lowest level (*10, 16*). The experiments conducted with AntBot were performed at any time of the day (Table S6 and S7). (iii) The methods used by desert ants to estimate the distance travelled differ considerably from those classically adopted in rovers (involving wheel encoders). The legged AntBot robot mimics desert ants in many respects: the morphological and locomotor aspects, the visual heading measurements, the odometric process based on the OF and the stride integration; and the PI processes on which their homing navigation is based. AntBot can reach very low homing errors such as that of only 0.47% (*i.e.*, 6.47cm) after taking a 14m-long trajectory, as shown in Fig. 1B. The stride information can also be used to determine the robot's heading reliably (modes PI-OF-ST and PI-ST-FUSE). The five modes tested all effect a decorrelation between the stride-counting (ST) and the optic flow measurements (OF), which is interesting from the biological point of view. AntBot's navigation performances are particularly impressive in view of the very small number of pixels involved in comparison with traditional engineering solutions (up to several megapixels in the case of both OF sensors and celestial compasses).

The homing criterion adopted in this study was the ability to reach an area with a radius corresponding to half of AntBot's diameter. Due to the robot's walking and turning limitations (maximum walking stride 8.2cm, maximum turning stride 10.9°), this criterion was a fair compromise between AntBot's possibilities and the requirements of the homing task. The probability density of the homing error was studied in the case of all the PI modes tested. All the PI modes were found to have normal distributions (Fig. 5 and 6). On the other hand, the angular drift and the stride length also resulted in normal distributions, as shown in Fig. S12. The use of several Kalman filters may therefore improve the robot's homing performances in the PI-Full mode: the first filter could be applied to the stride-based estimate of both the heading angle and the travel distance; and the second filter could be applied directly to the PI procedure.

In its present form, AntBot has a diameter of 45cm and walked at a speed of approximately 10cm/s during the experiments, whereas *Cataglyphis fortis* desert ants are only 1cm long. As shown in Fig. 1A, the ant's trajectory measured 732.6m. AntBot should therefore have covered more than 32km to be properly compared with ants' navigation performances. Although AntBot can walk at speeds of up to 90cm/s, very large-scale navigation will require improving the hexapod robot's actuators and power supply. This will make it possible to test the PI-Full mode in more natural contexts such as rugged

terrains in a cluttered environment (forests) where the view of the sky is often barred by the presence of branches and leaves in the visual field of the celestial compass. The possibility of using the celestial compass under a forest canopy may require further visual processing of the POL-units' signals: it is planned, for example, to investigate the effects of the phase of the signals on the AoP calculations.

The PI process adopted by *Cataglyphis* desert ants was embedded on-board a fully ant-inspired hexapod walking robot which mimics both the insect's shape and the visual sensory modes involved. This approach yielded outstanding performances in several homing tasks. Yet, as shown in Fig. 1, desert ants are perfectly able to make their way back to their nest, while AntBot is still subject to a residual homing error of 0.47%. This difference can be explained by the VG used by desert ants during the final approach to their nest, as well as by the combination with PI adopted during their journey (*22*). Low-resolution panoramic vision is needed to perform VG navigation, but also to add the collision avoidance skills needed to make the robot more adapted to unknown, uneven environments where obstacles are liable to occur. The robot's static friction coefficient has been found to be equal to 0.35, corresponding to a minimum ground slope of approximately 20°. Further experiments should consequently focus on the robot's homing performances when walking on more steeply sloping ground.

Materials and Methods

The navigation task used in this paper was a homing task performed after a random trajectory in a flat outdoor environment. The low computational-cost ant-inspired approach presented here, which requires just a few sensors, considerably improved the robot's homing performances. To meet this challenge, our hexapod robot AntBot was equipped with a celestial compass mimicking ants' DRA, which determines the robot's heading angle, and the M²APix OF sensor, which collects the ventral OF cues ensuring precise odometric measurements. The robot is also capable of integrating its strides while walking straight ahead (thus obtaining additional odometric cues) and while turning (thus obtaining additional orientation cues). Five methods combining all these sensory modes were therefore compared in this study.

The robot's construction

AntBot is a fully 3-D printed structure (using polylactic acid (PLA) filament). The 3D parts are available at https://github.com/JuSquare/AntBot/tree/master/3D Parts. The robot is equipped with an Open CM 9.04C board, which is an Arduino-like microcontroller adapted for use with Dynamixel servos via a transistor-transistor logic (TTL) serial communication (Fig. 2B). This controller includes an ARM Cortex-M3 processor. AntBot's legs have three degrees of freedom controlled by Dynamixel AX-18 servos. The embedded micro-computer unit is a Raspberry Pi 2 Model B including a 900MHz quad core ARM Cortex-A7 CPU with 1 GB memory. A board shield was designed in order to plug all the sensors and electronic devices onto the micro-computer unit. Communications between AntBot and the host computer took place via a local WiFi network. The robot is powered by a three-cell 11.4V 5300mAh lithium polymer battery (Gens ACE) mounted below the robot.

The optical compass

The celestial compass consists of two UV-polarized light sensors called POL-units, the spectral sensitivity of which ranges from 270nm to 400nm, with a peak transmission at 330nm. Each POL-unit is composed of a UV-sensitive photodiode SG01D-18 (*SgLux*) topped with a UV linear sheet polarizer (HNP'B replacement) held by a gear driven by a stepper motor AM0820-A-0.225-7 (*Faulhaber*) (Fig. 3BC and S2). This motor is controlled by the Raspberry Pi 2 board via an I2C communication protocol. Two custom-made Hall-effect sensors signal each full rotation completed by the gears (Fig. S3C). The sensor is 3D-printed using PLA filament. The parts are available at: https://github.com/JuSquare/AntBot/tree/master/CelestialCompass.

The optical compass was fully characterized. The noise level was quantified, and the results show that POL-units feature Gaussian noise (Fig. S4). The angular aperture of each POL-unit is equal to ±60° centered at 90° (Fig. S3). The effects of clouds were investigated (Fig. S5 and S6). The celestial compass RMSE under clear sky conditions (all UV-indexes combined) was equal to 1.3%. This error dropped to 10.3% under a covered sky, but field results showed that the short-range navigation performances were still satisfactory (*65*). The pattern of polarization had to remain fairly constant during the insect's or robot's journey. In practice, the present experiments did not take longer than 20 minutes, which was consistent with the duration of the insects' journey.

Given the regular pattern of skylight polarization (Fig. 3A), the output of each POL-unit is a 180° periodic sine wave, with a 180° shift between the two POL-units as the linear sheet polarizers are set orthogonally to each other. Raw signals are low-pass filtered and normalized (Fig. 3D). The log-ratio output is then calculated between the two normalized and corrected signals (Fig. 3E), from which the robot's heading angle is then determined. Due to the symmetry of the polarization pattern, this angle of orientation is known to range within [0°;180°]. To solve the solar / anti-solar ambiguity, AntBot rolls its celestial compass to detect the half (right or left) of the sky containing the maximum UV level (Fig. S7). Lastly, the effect of the sun's course on the polarization is corrected after the solar ephemerides have been collected online (https://www.sunearthtools.com/) in order to specify the exact location and dates of the experiments.

The optic flow sensor

The ventral OF sensor embedded on board AntBot is a M²APix (*66*) including 12 hexagonal Michaelis-Menten pixels (Fig. 4). The inter-receptor angle was found to be equal to 3.57° with a standard deviation of 0.027° (Fig. S8). One OF value is computed by two adjacent pixels in a row, giving the time lag between the two pixels' detection of a single moving contrast, based on the cross-correlation method (Text S2). The 10 local OF values are then sorted and those which do not fit a specific range (defined on the basis of AntBot's typical speed) are removed. The final OF is calculated, taking the mean value of all the remaining OF values. Lastly, the travel distance is computed based on this mean OF value.

Collecting the ground truth data

The indoor experiments were recorded using our motion capture system, consisting of 17 infrared VICON^{TM} cameras placed in a 6m x 6m x 8m flight arena to determine the robot's 3-D location with millimetric precision. At each checkpoint, the robot's location is tracked and stored in a Matlab file. The outdoor experiments were recorded by taking photographs of the scene at each checkpoint. The perspective was then corrected in each

photograph and a point-and-click application was coded in Matlab language to determine the location of the robot in its environment. The robot's distance from the goal was also measured directly during all the outdoor experiments, before and after the homing trip. The overall results of all the experiments were processed with Matlab software.

References and Notes

1. K. Kovach, P. J. Mendicki, E. D. Powers, B. Renfro, GPS Receiver Impact from the UTC Offset (UTCO) Anomaly of 25-26 January 2016. *Proceedings of 29th ION GNSS* (2016).
2. M. J. Milford, G. F. Wyeth, in *2012 IEEE International Conference on Robotics and Automation* (IEEE, 2012), pp. 1643–1649.
3. S. Weiss, D. Scaramuzza, R. Siegwart, Monocular-SLAM–based navigation for autonomous micro helicopters in GPS-denied environments. *J. Field Robot.* **28**, 854–874 (2011).
4. Y. Ham, K. K. Han, J. J. Lin, M. Golparvar-Fard, Visual monitoring of civil infrastructure systems via camera-equipped Unmanned Aerial Vehicles (UAVs): a review of related works. *Visualization in Engineering*. **4**, 1 (2016).
5. S. Lowry *et al.*, Visual Place Recognition: A Survey. *IEEE Trans. Robot.* **32**, 1–19 (2016).
6. A. R. Vidal, H. Rebecq, T. Horstschaefer, D. Scaramuzza, Ultimate SLAM? Combining Events, Images, and IMU for Robust Visual SLAM in HDR and High-Speed Scenarios. *IEEE Robot. Autom. Lett.* **3**, 994–1001 (2018).
7. E. Mueggler, H. Rebecq, G. Gallego, T. Delbruck, D. Scaramuzza, The event-camera dataset and simulator: Event-based data for pose estimation, visual odometry, and SLAM. *Int. J. Robot. Res.* **36**, 142–149 (2017).
8. M. Fallon, Accurate and robust localization for walking robots fusing kinematics, inertial, vision and LIDAR. *Interface Focus*. **8** (2018).
9. Y. Zhao, Applying Time-Differenced Carrier Phase in Nondifferential GPS/IMU Tightly Coupled Navigation Systems to Improve the Positioning Performance. *IEEE Trans. Vehic. Tech.* **66**, 992–1003 (2017).
10. R. Wehner, S. Wehner, Insect navigation: use of maps or Ariadne's thread? *Ethology Ecology & Evolution*. **2**, 27–48 (1990).
11. B. Webb, What does robotics offer animal behaviour? *Animal Behaviour*. **60**, 545–558 (2000).
12. N. Franceschini, Small Brains, Smart Machines: From Fly Vision to Robot Vision and Back Again. *Proc. IEEE*. **102**, 751–781 (2014).
13. R. Wehner, B. Michel, P. Antonsen, Visual navigation in insects: coupling of egocentric and geocentric information. *J. Exp. Biol.* **199**, 129–140 (1996).
14. R. Wehner, The Desert Ant's Navigational Toolkit: Procedural Rather than Positional Knowledge. *Navigation*. **55**, 101–114 (2008).
15. A. Vardy, R. Moller, Biologically plausible visual homing methods based on optical flow techniques. *Connection Science*. **17**, 47–89 (2005).
16. M. Collett, T. S. Collett, S. Bisch, R. Wehner, Local and global vectors in desert ant navigation. *Nature*. **394**, 269 (1998).
17. M. O. Franz, B. Schölkopf, H. A. Mallot, H. H. Bülthoff, Where did I take that snapshot? Scene-based homing by image matching. *Biol. Cyber.* **79**, 191–202 (1998).
18. M. Müller, R. Wehner, Path integration in desert ants, Cataglyphis fortis. *Proc. Natl. Acad. Sci.* **85**, 5287–5290 (1988).
19. M. Collett, T. S. Collett, How do insects use path integration for their navigation? *Biol. Cyber.* **83**, 245–259 (2000).
20. R. Wehner, Desert ant navigation: how miniature brains solve complex tasks. *J. Comp. Physiol. A.* **189**, 579–588 (2003).

21. S. Heinze, A. Narendra, A. Cheung, Principles of Insect Path Integration. *Curr. Biol*. **28**, R1043–R1058 (2018).
22. R. Wehner, T. Hoinville, H. Cruse, K. Cheng, Steering intermediate courses: desert ants combine information from various navigational routines. *J. Comp. Physiol. A.* **202**, 459–472 (2016).
23. E. L. G. Legge, A. Wystrach, M. L. Spetch, K. Cheng, Combining sky and earth: desert ants (Melophorus bagoti) show weighted integration of celestial and terrestrial cues. *J. Exp. Biol*. **217**, 4159–4166 (2014).
24. A. Wystrach, M. Mangan, B. Webb, Optimal cue integration in ants. *Proc. Roy. Soc. London B: Biol. Sci*. **282** (2015).
25. P. Duelli, R. Wehner, The spectral sensitivity of polarized light orientation in Cataglyphis bicolor (Formicidae, Hymenoptera). *J. Comp. Physiol. A*. **86**, 37–53 (1973).
26. T. Labhart, The electrophysiology of photoreceptors in different eye regions of the desert ant, Cataglyphis bicolor. *J. Comp. Physiol. A*. **158**, 1–7 (1986).
27. R. Wehner, in *Orient. Comm. Arthropods*, M. Lehrer, Ed. (Birkhäuser Basel, Basel, 1997), pp. 145–185.
28. R. Wehner, M. Müller, The significance of direct sunlight and polarized skylight in the ant's celestial system of navigation. *Proc. Natl. Acad. Sci*. **103**, 12575–12579 (2006).
29. T. Labhart, E. P. Meyer, Detectors for polarized skylight in insects: a survey of ommatidial specializations in the dorsal rim area of the compound eye. *Micro. Res. Tech*. **47**, 368–379 (1999).
30. M. L. Brines, J. L. Gould, Skylight Polarization patterns and Animal Orientation. *J. Exp. Biol*. **96**, 69–91 (1982).
31. A. Barta, G. Horváth, Why is it advantageous for animals to detect celestial polarization in the ultraviolet? Skylight polarization under clouds and canopies is strongest in the UV. *J. Theor. Biol*. **226**, 429–437 (2004).
32. G. Horváth, D. Varjú, *Polarized Light in Animal Vision* (Springer Berlin Heidelberg, 2004).
33. R. Wehner, M. Müller, How do ants acquire their celestial ephemeris function? *Naturwissenschaften*. **80**, 331–333 (1993).
34. F. C. Dyer, J. A. Dickinson, Development of Sun Compensation by Honeybees: How Partially Experienced Bee Estimate the Sun's Course. *Proc. Natl. Acad. Sci*. **91**, 4471–4474 (1994).
35. K. Pfeiffer, U. Homberg, Coding of Azimuthal Directions via Time-Compensated Combination of Celestial Compass Cues. *Curr. Biol*. **17**, 960–965 (2007).
36. M. Bech, U. Homberg, K. Pfeiffer, Receptive Fields of Locust Brain Neurons Are Matched to Polarization Patterns of the Sky. *Curr. Biol*. **24**, 2124–2129 (2014).
37. T. Labhart, Polarization-opponent interneurons in the insect visual system. *Nature*. **331**, 435–437 (1988).
38. D. Lambrinos *et al.*, An Autonomous Agent Navigating with a Polarized Light Compass. *Adaptive Behavior*. **6**, 131–161 (1997).
39. J. Chu, K. Zhao, Q. Zhang, T. Wang, Construction and performance test of a novel polarization sensor for navigation. *Sensors and Actuators A: Physical*. **148**, 75–82 (2008).
40. D. Lambrinos, R. Möller, T. Labhart, R. Pfeifer, R. Wehner, A mobile robot employing insect strategies for navigation. *Robot. Autom. Sys*. **30**, 39–64 (2000).
41. J. Chu *et al.*, Integrated Polarization Dependent Photodetector and Its Application for Polarization Navigation. *IEEE Photon. Tech. Lett*. **26**, 469–472 (2014).
42. S. Karman, S. Diah, I. Gebeshuber, Bio-Inspired Polarized Skylight-Based Navigation Sensors: A Review. *Sensors*. **12**, 14232–14261 (2012).

43. J. Chahl, A. Mizutani, Biomimetic Attitude and Orientation Sensors. *IEEE Sensors J.* **12**, 289–297 (2012).
44. H. G. Krapp, Ocelli. *Curr. Biol.* **19**, R435–R437 (2009).
45. C. Fan, X. Hu, J. Lian, L. Zhang, X. He, Design and Calibration of a Novel Camera-Based Bio-Inspired Polarization Navigation Sensor. *IEEE Sensors J.* **16**, 3640–3648 (2016).
46. T. York *et al.*, Bioinspired Polarization Imaging Sensors: From Circuits and Optics to Signal Processing Algorithms and Biomedical Applications. *Proc. IEEE.* **102**, 1450–1469 (2014).
47. Y. Wang *et al.*, Design of a Device for Sky Light Polarization Measurements. *Sensors*. **14**, 14916–14931 (2014).
48. W. Zhang, Y. Cao, X. Zhang, Z. Liu, Sky light polarization detection with linear polarizer triplet in light field camera inspired by insect vision. *Appl. Opt.* **54**, 8962–8970 (2015).
49. J. Chu, H. Wang, W. Chen, R. Li, in *Proc. of International Conference on Mechatronics and Automation* (IEEE, 2009), pp. 3763–3768.
50. M. V. Srinivasan, Going with the flow: a brief history of the study of the honeybee's navigational `odometer'. *J. Comp. Physiol. A.* **200**, 563–573 (2014).
51. B. A. Cartwright, T. S. Collett, Landmark learning in bees. *J. Comp. Physiol*. **151**, 521–543 (1983).
52. J. Zeil, M. I. Hofmann, J. S. Chahl, Catchment areas of panoramic snapshots in outdoor scenes. *J. Opt. Soc. Am. A.* **20**, 450–469 (2003).
53. A. Wystrach, G. Beugnon, K. Cheng, Landmarks or panoramas: what do navigating ants attend to for guidance? *Frontiers Zoo*. **8**, 21 (2011).
54. P. Graham, K. Cheng, Ants use the panoramic skyline as a visual cue during navigation. *Curr. Biol*. **19**, R935–R937 (2009).
55. B. Ronacher, R. Wehner, Desert ants Cataglyphis fortis use self-induced optic flow to measure distances travelled. *J. Comp. Physiol. A.* **177**, 21–27 (1995).
56. S. Wohlgemuth, B. Ronacher, R. Wehner, Ant odometry in the third dimension. *Nature*. **411**, 795 (2001).
57. M. Wittlinger, R. Wehner, H. Wolf, The Ant Odometer: Stepping on Stilts and Stumps. *Science*. **312**, 1965–1967 (2006).
58. M. Wittlinger, R. Wehner, H. Wolf, The desert ant odometer: a stride integrator that accounts for stride length and walking speed. *J. Exp. Biol*. **210**, 198–207 (2007).
59. M. Knaden, P. Graham, The Sensory Ecology of Ant Navigation: From Natural Environments to Neural Mechanisms. *Annual Rev. Entomo*. **61**, 63–76 (2016).
60. S. E. Pfeffer, M. Wittlinger, Optic flow odometry operates independently of stride integration in carried ants. *Science*. **353**, 1155–1157 (2016).
61. A. Cully, J. Clune, D. Tarapore, J.-B. Mouret, Robots that can adapt like animals. *Nature*. **521**, 503 (2015).
62. C. Zollikofer, Stepping patterns in ants - Influence of speed and curvature. *J. Exp. Biol*. **192**, 95–106 (1994).
63. D. Graham, A behavioural analysis of the temporal organisation of walking movements in the 1st instar and adult stick insect (Carausius morosus). *J. Comp. Physiol*. **81**, 23–52 (1972).
64. J. Dupeyroux, J. Diperi, M. Boyron, S. Viollet, J. Serres, in *2017 European Conference on Mobile Robots (ECMR)* (IEEE, 2017), pp. 1–6.
65. J. Dupeyroux, S. Viollet, J. Serres, Polarized skylight-based heading measurements: a bio-inspired approach. J. R. Soc. Interface (2019).
66. S. Mafrica *et al.*, A bio-inspired analog silicon retina with Michaelis-Menten auto-adaptive pixels sensitive to small and large changes in light. *Opt. Express*. **23**, 5614–5635 (2015).
67. S. Mafrica, A. Servel, F. Ruffier, Minimalistic optic flow sensors applied to indoor and outdoor visual guidance and odometry on a car-like robot. *Bioinsp. Biomim*. **11**, 066007 (2016).

68. K. L. Coulson, Characteristics of the radiation emerging from the top of a rayleigh atmosphere—I: Intensity and polarization. *Planet. Space Sci*. **1**, 265–276 (1959).
69. K. L. Coulson, *Polarization and Intensity of Light in the Atmosphere* (A Deepak Pub, 1988).
70. U. Pegel, K. Pfeiffer, U. Homberg, Integration of celestial compass cues in the central complex of the locust brain. *J. Exp. Biol*. **221** (2018).
71. J. Dupeyroux, G. Passault, F. Ruffier, S. Viollet, J. Serres, in *IFAC Word Congress 2017* (2017), pp. 1628–1631.

Acknowledgements

Acknowledgements: The authors would like to thank Marc Boyron and Julien Diperi for their technical support with designing the celestial compass, Sean Lapalus for his help with the outdoor experimental setup, and Jessica Blanc for revising the English manuscript.

Funding: This research was supported by the French Direction Générale de l'Armement (DGA), CNRS, Aix Marseille Université, the Provence-Alpes-Côte d'Azur region, and the French National Research Agency for Research (ANR) in the framework of the Equipex/Robotex project.

Authors' contributions: JD and JS designed the robot; JD built the robot; JD, JS and SV designed the celestial compass, JD designed the software and conducted the experiments; JD, JS and SV interpreted the data; JD wrote the original draft; JD, JS and SV revised the manuscript; JS and SV supervised the project.

Competing interests: The authors have no conflicts of interest to declare.

Data and materials availability: The 2-D trajectories' datasets in Matlab files are available online at: https://github.com/JuSquare/AntBot/tree/master/Experiments.

Figures and Tables

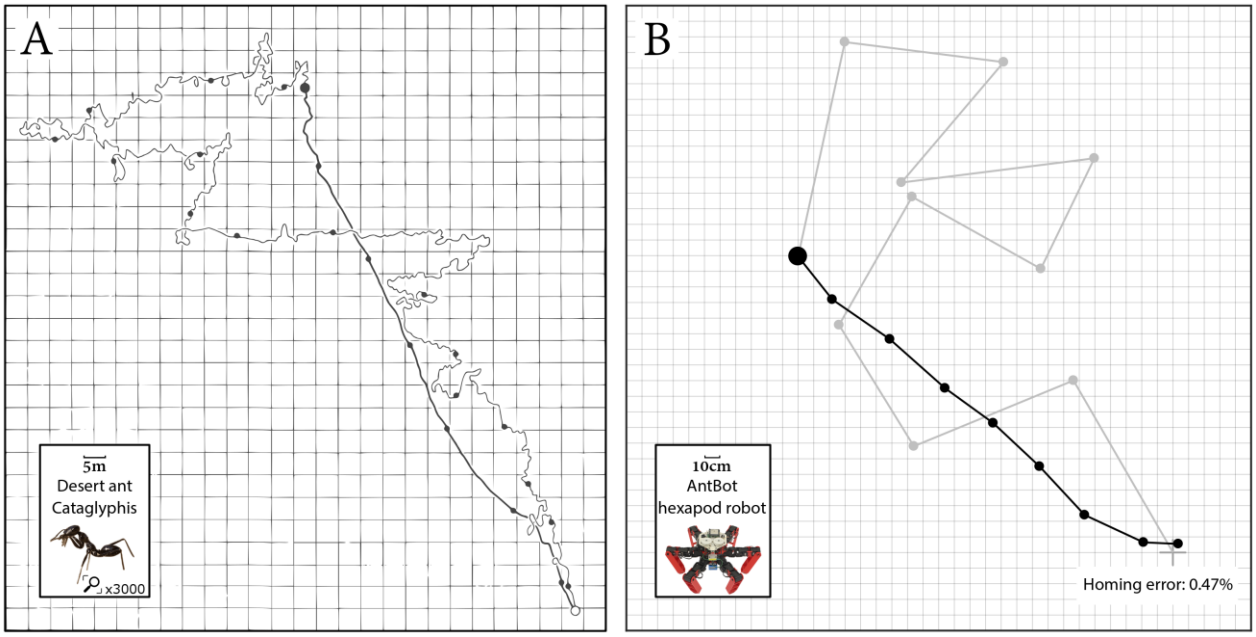

Fig. 1. Homing trajectories of the desert ant *Cataglyphis* and the AntBot hexapod robot. (A) Path integration in the desert ant *Cataglyphis fortis*. After a random-like outbound trajectory (thin line 592.1m long), the forager went straight back to its nest (thick line 140.5m-long). Open circle marks the nest entrance, and the large filled one shows the feeding location. Small filled dots represent time marks (every 60s). Adapted from (*10*) by permission of Taylor & Francis. **(B)** AntBot's homing performances inspired by experiments on *Cataglyphis* desert ants in (A). After a 10-checkpoint outbound trajectory (gray line 10.6m long), AntBot went back to its starting-point (gray cross) just like desert ants (black line 3.2m-long). Solid points denote the checkpoints where AntBot stopped to determine its heading.

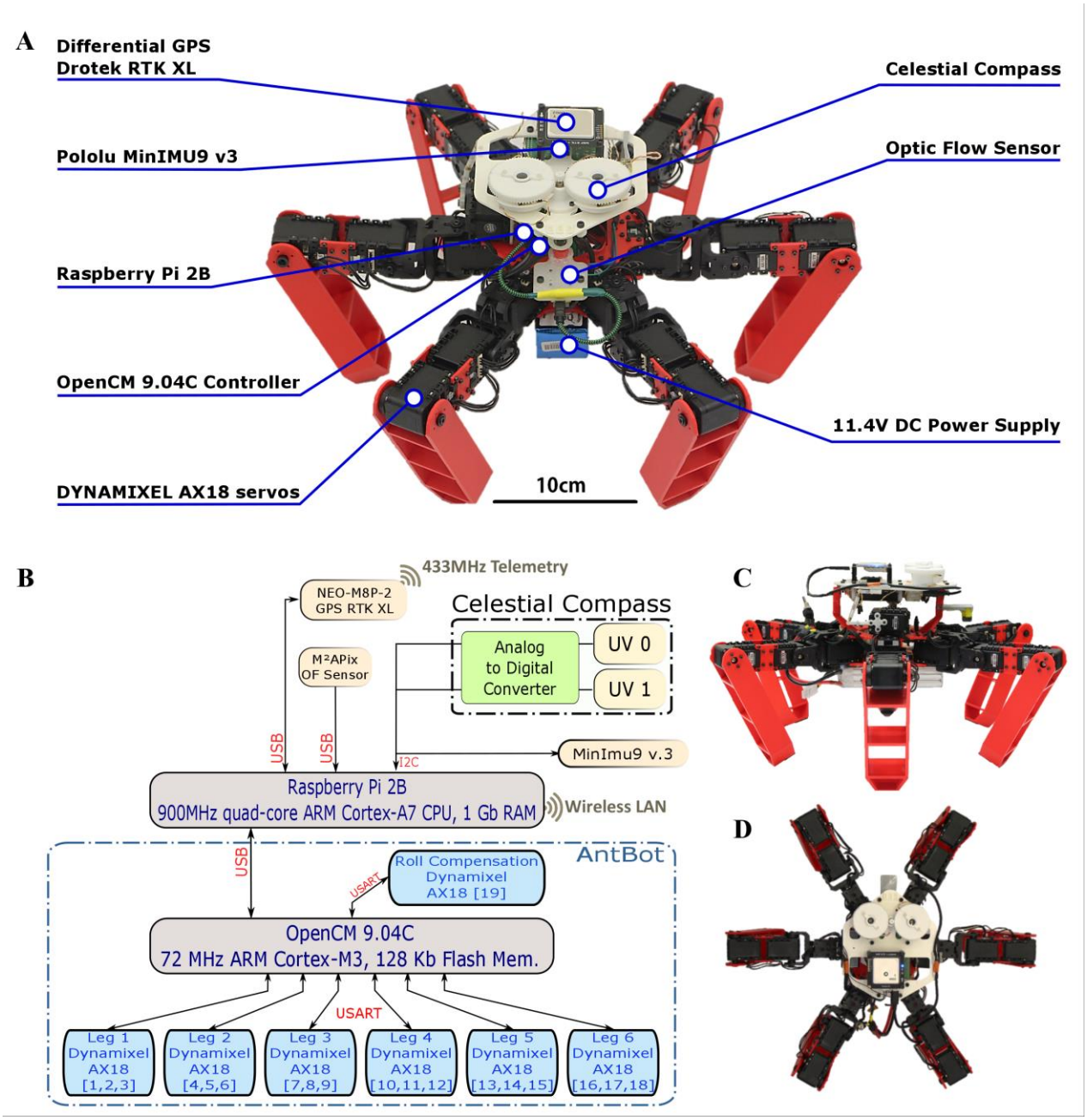

Fig. 2. Hardware used in the hexapod robot AntBot. (A) Structure of the robot with its sensors and electronic parts. **(B)** Hardware architecture of the AntBot robotic platform. To deal with the communications between the Raspberry Pi 2B board and the other electronic devices (the celestial compass, IMU (MinImu9 v.3), M²APix optic flow sensor, and stepper motor), a custom-made shield was developed. **(C)** Side and **(D)** top views of AntBot.

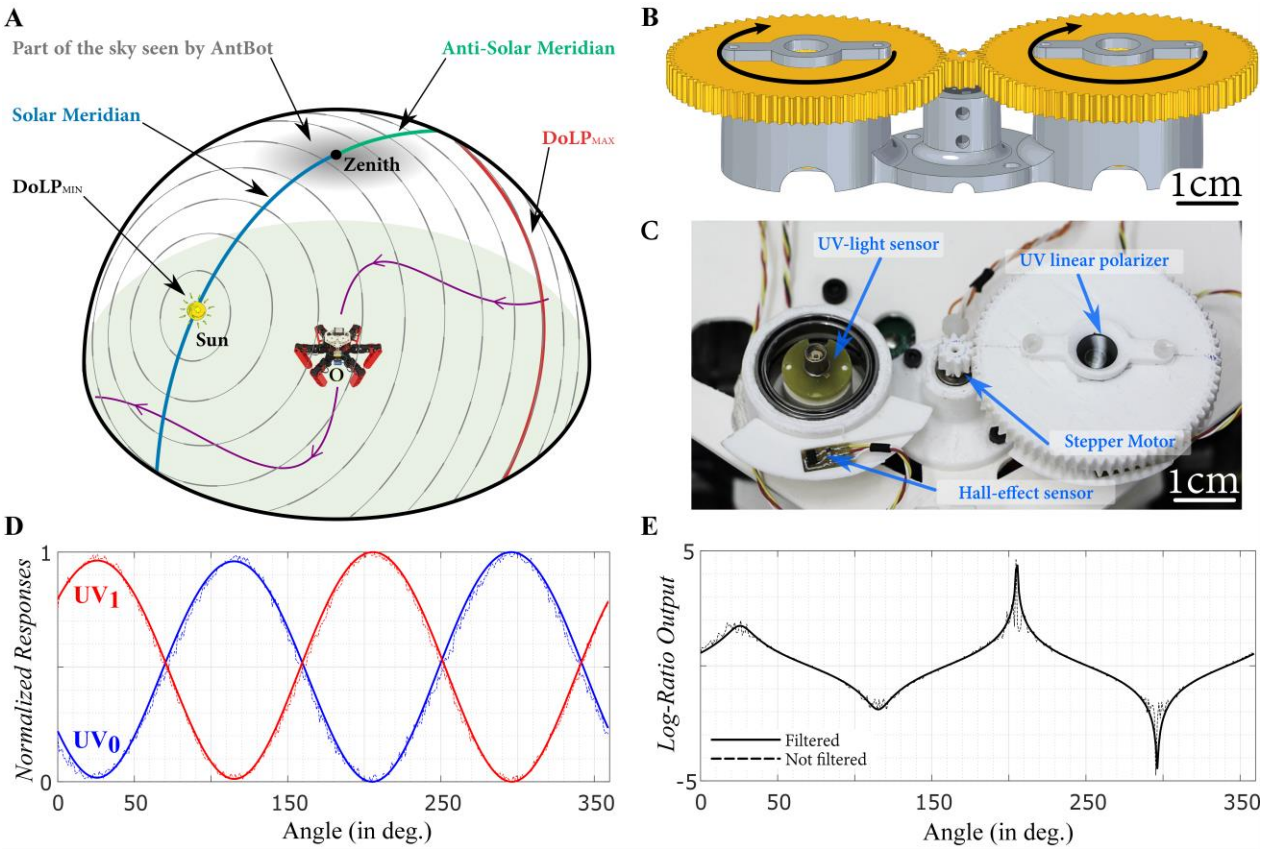

Fig. 3. The celestial compass. (A) Three-dimensional diagram of the pattern of polarization in the sky relative to the AntBot robot observer (O), at a given elevation of the sun. The gray curves give the angle of polarization all around the dome of the sky. The minimum degree of linear polarization (DoLP) occurs in the region of the sun, and the maximum, 90° from the sun (red curve). **(B)** Computer-aided design view of the celestial compass. **(C)** Photograph of the celestial compass. On the left, the top gear has been removed to show the UV-light sensor and the Hall-effect sensor used to stop the sky scanning process after one full gear rotation. **(D)** An example of normalized raw (thin lines) and filtered (thick lines) signals UV_0 (in blue) and UV_1 (in red) during a sunny day in April 2017 in Marseille, France. **(E)** Raw (thin line) and filtered (thick line) log-ratio signals between UV_0 and UV_1. The angle of polarization is located at the minimum values of the log-ratio output (here, the AoP is 118° mod 180°).

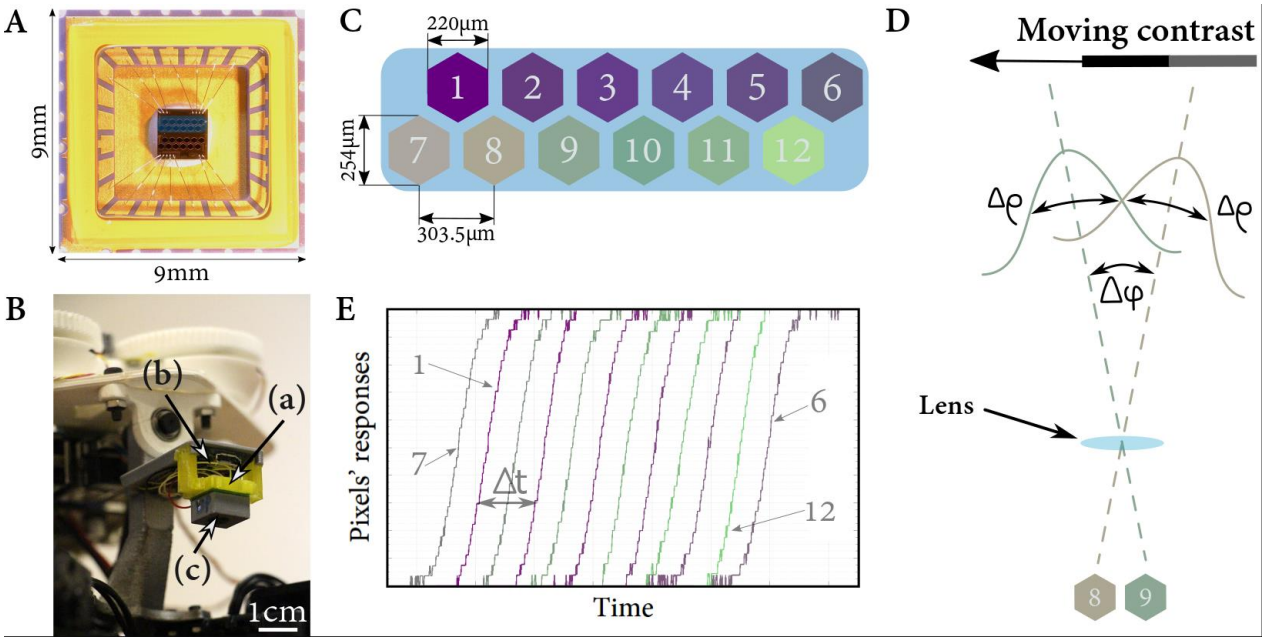

Fig. 4. AntBot's ventral optic flow sensor. (A) The M²APix silicon retina. Adapted from (*66*). The OF sensor is composed of 12 Michaelis-Menten pixels. **(B)** Photograph of the M²APix OF sensor embedded on board AntBot. The sensor (a) is connected to a Teensy 3.2 microcontroller (b) and topped with a Raspberry Pi NoIR defocused lens (c). **(C)** Schematic view of the 12 Michaelis-Menten hexagonal pixels, divided into two rows of 6 pixels. **(D)** Optic geometry of a local motion sensor: two adjacent pixels in a row, showing visual signal acquisition of a moving contrast, depending on the inter-pixel angle $\Delta\varphi$ between two adjacent pixels and the acceptance angle $\Delta\rho$ corresponding to the width of the Gaussian angular sensitivity of each pixel at half height. **(E)** Example of raw signals generated by a black/white moving edge. The colors correspond to those used in (C). The time lag between two adjacent pixels (Δt) is computed using cross-correlation methods.

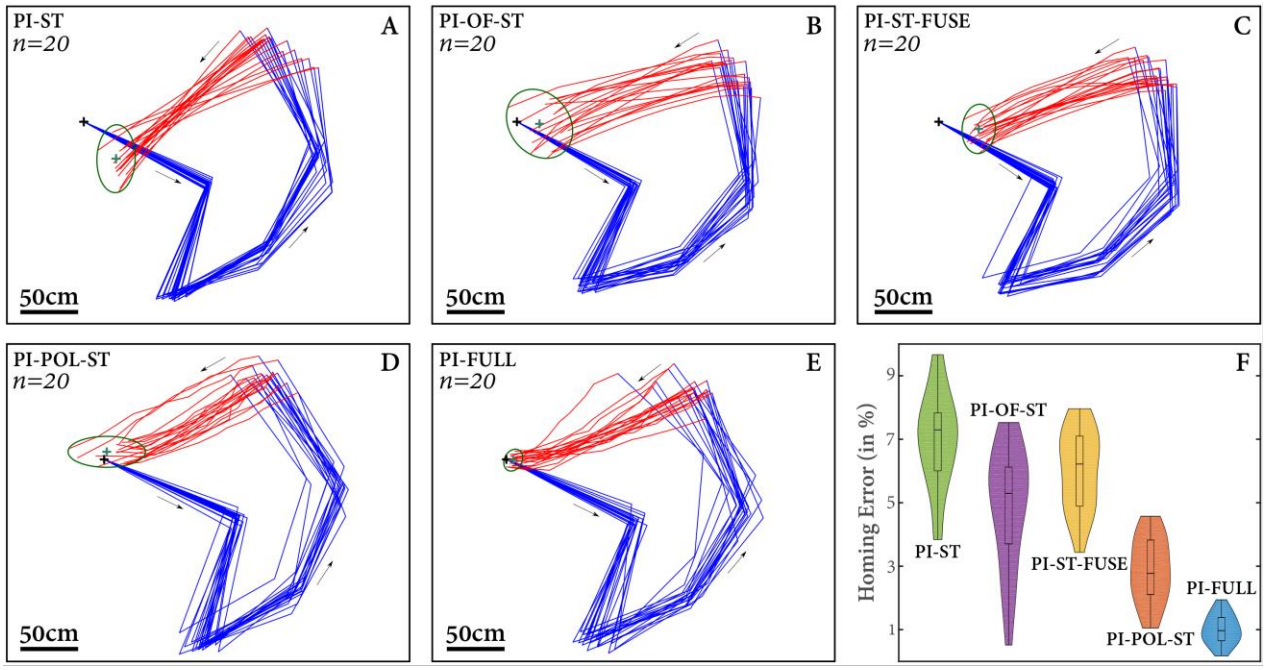

Fig. 5. Homing performances on a 5-checkpoint trajectory. (A-E) Homing results on the 5-checkpoint trajectory based on the PI mode. The trajectory was repeated 20 times. Blue lines give the outbound trajectory, and red lines, the homeward trajectory. The black cross symbolizes the home location, and the green cross is the average position of AntBot after homing. **(F)** Box and violin plots of the homing error as a percentage of the entire journey in each PI mode. Violin plots show the probability density corresponding to each error value.

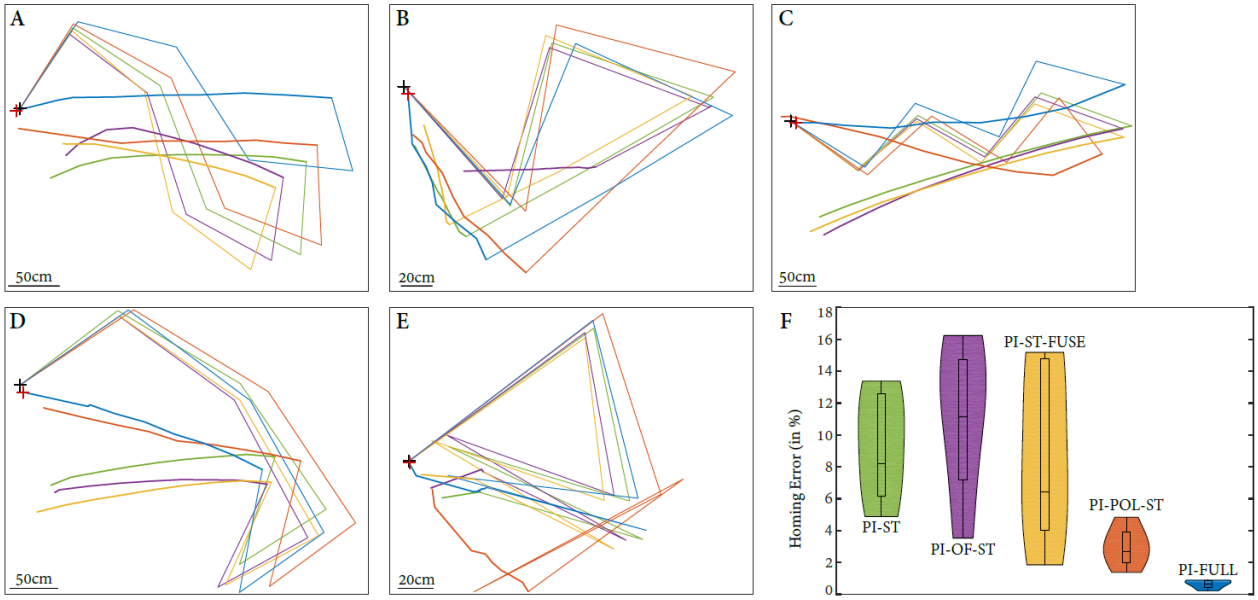

Fig. 6. AntBot's homing performances in 5 different 5-checkpoint trajectories. (A-E) The five trajectories tested. Outbound trajectories are presented in thin lines and homeward trajectories, in thick lines. **(F)** Box and violin plots of the 5 trajectories in all the PI modes tested. Violin plots show the probability density corresponding to each error value with each of the PI methods tested.

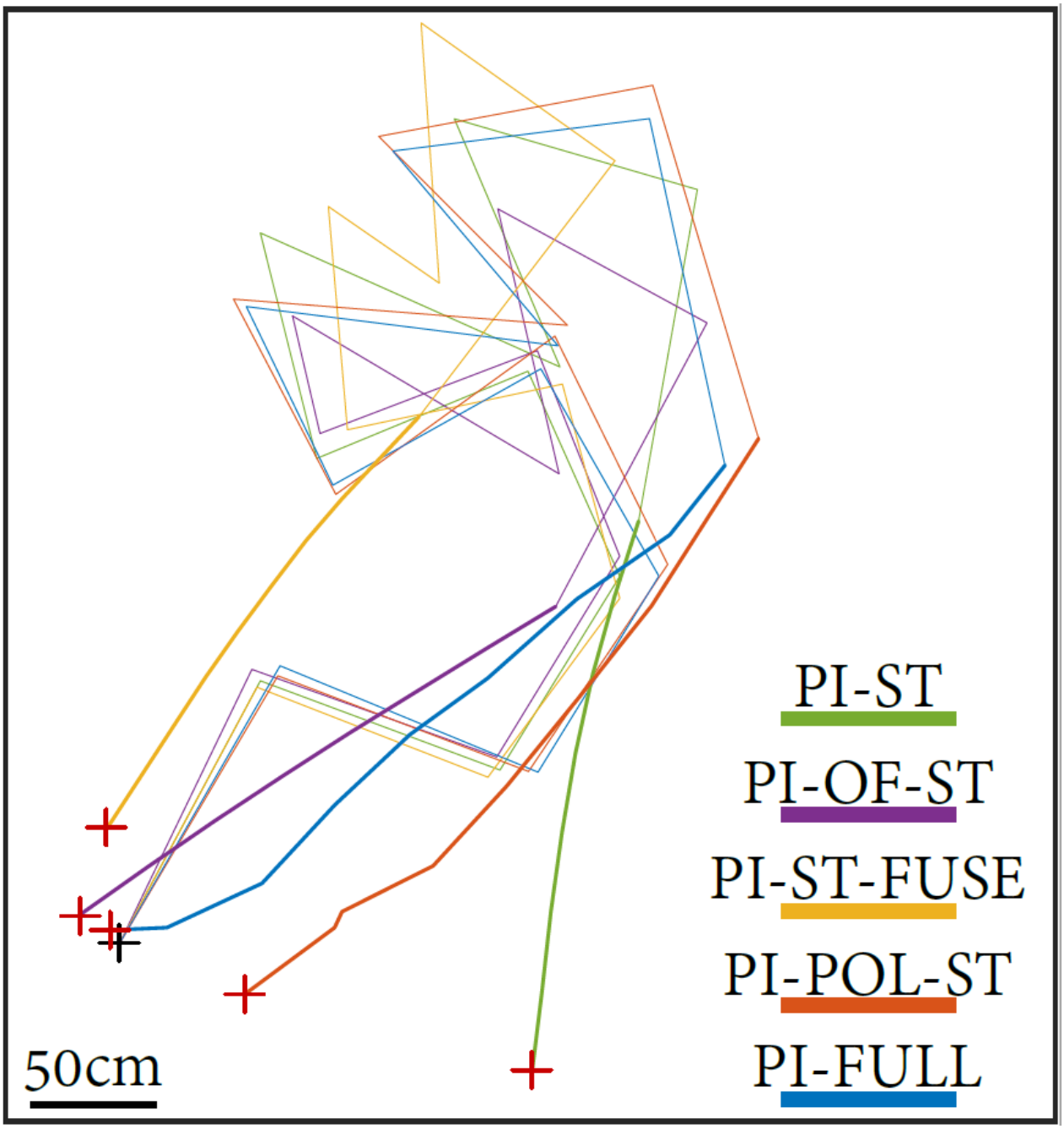

Fig. 7. AntBot's homing performances involving a long trajectory. The black cross gives the starting-point; the red crosses give the homing result in each of the PI modes tested. Outbound trajectories are presented in thin lines and homeward trajectories, in thick lines.

A

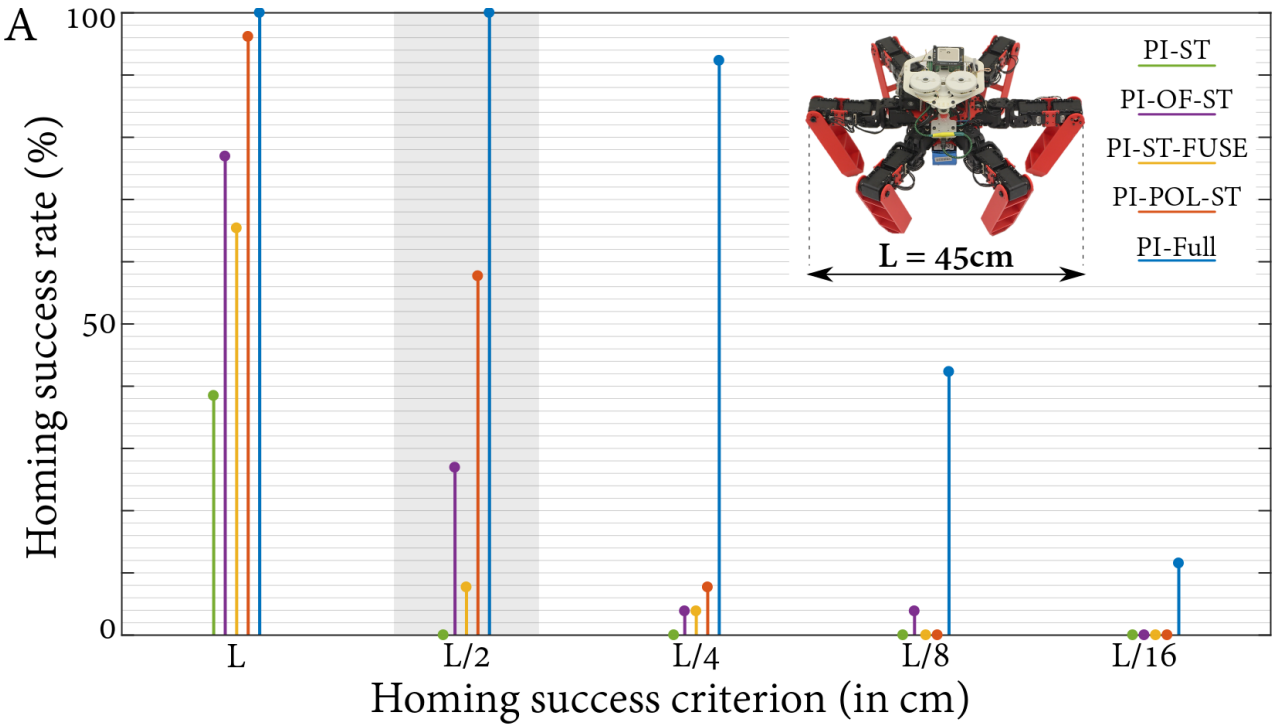

B

Path Integration Mode	Trajectory repeated 20 times	Random trajectory 1	Random trajectory 2	Random trajectory 3	Random trajectory 4	Random trajectory 5	10-checkpoints trajectory	Mean	Standard Deviation
PI-ST	7.29%	9.57%	6.81%	13.37%	12.21%	4.87%	13.44%	9.65%	3.45%
PI-OF-ST	5.30%	8.99%	13.94%	16.23%	13.32%	3.53%	1.55%	8.98%	5.69%
PI-ST-FUSE	6.22%	7.77%	5.10%	15.18%	14.61%	1.85%	4.05%	7.83%	5.17%
PI-POL-ST	2.77%	2.31%	4.83%	1.38%	3.45%	3.00%	3.77%	3.07%	1.10%
PI-Full	0.97%	0.51%	0.88%	0.77%	0.86%	0.22%	0.47%	0.67%	0.27%

Fig. 8. Homing performances of AntBot. (A) Homing success rate based on the homing success criterion defined as a fraction of the robot's diameter (L). The criterion used in this study was L/2. **(B)** Homing errors as a percentage of the entire trajectory, depending on the path integration modes described in Fig. 5 and Fig. 6. The mean errors and standard deviations were based on all the results obtained in the 26 experiments.

SUPPLEMENTARY MATERIALS

Supplementary materials for:

AntBot, a six-legged walking robot able to home like desert ants in outdoor environments

Julien Dupeyroux, Julien Serres, Stéphane Viollet*

* Corresponding author. Email: stephane.viollet@univ-amu.fr

The PDF file includes:

Other Supplementary Materials for this manuscript include the following:

Movie S1 (.mp4 format). AntBot's homing performance in the PI-ST mode.
Movie S2 (.mp4 format). AntBot's homing performance in the PI-OF-ST mode.
Movie S3 (.mp4 format). AntBot's homing performance in the PI-ST-FUSE mode.
Movie S4 (.mp4 format). AntBot's homing performance in the PI-POL-ST mode.
Movie S5 (.mp4 format). AntBot's homing performance in the PI-FULL mode.

Summary of path integration modes:

PI-ST	Odometry: strides	Orientation: strides.
PI-OF-ST	Odometry: optic flow	Orientation: strides.
PI-ST-FUSE	Odometry: optic flow & strides	Orientation: strides.
PI-POL-ST	Odometry: strides	Orientation: celestial compass.
PI-FULL	Odometry: optic flow & strides	Orientation: celestial compass.

Supplementary Text S1 – The celestial compass

UV_0 and UV_1 are the polarization units' responses, x is the rotation angle of the ultraviolet (UV) sheet polarizer, and ψ is the solar meridian angle. Depending on the UV-polarized light pattern, UV_0 and UV_1 are π-periodic sinusoids defined as follows:

$$\begin{cases} UV_0(x) = A_0 + B_0 \cos\big(2(x+\psi)\big) \\ UV_1(x) = A_1 + B_1 \cos\left(2\left(x+\psi+\frac{\pi}{2}\right)\right) \end{cases}, x \in [0;2\pi], \psi \in [0;\pi] \quad \text{(S1)}$$

Where A_0 and A_1 are the offsets caused by the ambient UV-light intensity and the inner bias of the photodiodes, and B_0 and B_1 are constant gains depending on the degree of polarization and the inner gain of each photodiode.

Raw polarization units' signals are low-pass filtered by applying the following method: all the values after the first harmonic in the Fourier transform, corresponding to the sine wave of maximum energy, are set at zero. The corrected signals are then normalized between $(0+\varepsilon)$ and 1, where $\varepsilon \ll 1$ in order to prevent the occurrence of log-ratio computation failure.

The celestial compass' response $p(x)$ is computed by taking the log-ratio between normalized and corrected signals, that is:

$$p(x) = log_{10}\left(\frac{UV_1^{nc}(x)}{UV_0^{nc}(x)}\right) \quad \text{(S1)}$$

Lastly, the solar meridian angle ψ is computed by locating the minima of the p function, first in $[0;\pi]$, and secondly in $[\pi;2\pi]$. Therefore, we have:

$$\psi = \frac{Res}{4}\left(\underset{x\in[0;\pi]}{\operatorname{argmin}}\, p(x) + \underset{x\in[\pi;2\pi]}{\operatorname{argmin}}\, p(x) + \underset{x\in[0;\pi]}{\operatorname{argmax}}\, p(x) + \underset{x\in[\pi;2\pi]}{\operatorname{argmax}}\, p(x) - \frac{\pi}{Res}\right) \quad \text{(S2)}$$

where Res is the angular resolution of the celestial compass, which is equal in this study to 0.96° (i.e. 0.0168 rad). To obtain ψ in $[0;2\pi]$, we simply refer to the position of the sun in the sky depending on the robot's longitudinal axis (rear – front), as described in Fig. S8. The orientation acquired ψ_i is determined between 0 and π due to the symmetry of the Rayleigh's scattering of sunlight. To disambiguate ψ_i, we used the celestial compass to determine the average UV levels in the left and right parts of the sky, depending on the robot's longitudinal axis (Fig. S8). This disambiguation procedure results in a value of ψ_i in $[0;2\pi]$.

The angular orientation of the robot ψ_i is corrected, based on the motion of the sun in the sky. Depending on the time elapsing since the first orientation computed ψ_{INIT}, the angular shift of the sun's elevation (contained in the solar ephemeris on the day of the experiment) is subtracted from the newly computed orientation ψ_i. The robot's orientation therefore ranges between 0 and 2π in the initial solar reference frame.

Supplementary Text S2 – The robot's odometer

With the methods based on stride integration, the distance $Dist_i$ walked by the robot is computed depending on the number of steps walked. Therefore, we have:

$$Dist_i = Stride_i \cdot d_{STRIDE} \tag{S3}$$

where d_{STRIDE} is the average distance covered per stride in cm, depending on the gait parameters applied, and $Stride_i$ is the number of strides performed. With the other methods, the distance covered $Dist_i$ is measured visually, using the ventral optic flow sensor M²APix. The optic flow *OF* in rad/s is defined as follows:

$$OF = \frac{\Delta\varphi}{\Delta T} \tag{S4}$$

where $\Delta\varphi$ is the inter-pixel angle between two adjacent pixels in a row, and ΔT is the time elapsing between the signals delivered by these two pixels. The time lag is estimated using the cross-correlation method between output signals from two adjacent (*66, 67*) pixels. To make this method more reliable, ΔT is defined as the mean of all the time lags estimated between each pair of adjacent pixels. If the distance d from the sensor to an object perceived in the scene is constant, then the linear speed V is given by:

$$V = d \cdot OF \tag{S5}$$

Taking $T_{STRIDE,i}$ to be the full walking time in seconds, then the distance $Dist_i$ covered between checkpoints $i-1$ and i will be:

$$Dist_i = \frac{d \cdot \Delta\varphi \cdot T_{STRIDE,i}}{\Delta T_i} \tag{S6}$$

The distance estimated in the PI-Full mode, based on both the ventral optic flow and the stride integration process, is computed as follows

$$Dist_i = \frac{1}{2}\left(Stride_i \cdot d_{STRIDE} + \beta \cdot \frac{d \cdot \Delta\varphi \cdot T_{STRIDE,i}}{\Delta T_i}\right) \tag{S8}$$

where β is an ad-hoc constant designed to compensate for any initial and final optic flow-based stride calculation errors, and to consider the difference of performance according to the temperature (morning: less than 8°C; afternoon: more than 10°C; see Table S2).

Supplementary Text S3 – The path integration process

We take ψ_{ROBOT} to denote the robot's orientation with respect to the X-axis, e.g. the transversal axis (left – right), ψ_{COMP} to denote the robot's orientation relative to the solar azimuth obtained with the robot's compass, ψ_{INIT} to denote the initial orientation given by the compass, and R to denote the turning angle. All the angular values are given in degrees. The robot's location is given at each checkpoint C_i by its (X_i, Y_i) position. Fig. S10 gives a geometrical view of the homing paths described here in the case of a 4-checkpoint trajectory.

In the initiation phase, the robot's longitudinal axis is aligned with the Y-axis. The robot's current orientation is then computed as follows at each checkpoint C_i, $i \in [1..\mathrm{N}]$:

$$\psi_{ROBOT,i} = \psi_{COMP,i} - \psi_{INIT} \tag{S9}$$

The corresponding turning motion R_i is defined as the difference between the current and previous orientations, that is:

$$R_i = \psi_{ROBOT,i} - \psi_{ROBOT,i-1} \tag{S10}$$

The robot then computes its current location (X_i, Y_i) relative to its departure point:

$$\begin{cases} X_i = X_{i-1} + Dist_i \cdot \cos\psi_{ROBOT,i} \\ Y_i = Y_{i-1} + Dist_i \cdot \sin\psi_{ROBOT,i} \end{cases} \tag{S11}$$

Where $Dist_i$ is the distance walked in cm from checkpoint C_{i-1} to checkpoint C_i. The homing distance $Dist_H$, in cm, and the direction ψ_H are computed as follows:

$$Dist_H = \sqrt{{X_N}^2 + {Y_N}^2} \tag{S12}$$

$$\psi_H = \begin{cases} atan\left(\frac{Y_N}{X_N}\right), & X_N < 0 \\ 180 + atan\left(\frac{Y_N}{X_N}\right), & X_N > 0 \end{cases} \tag{S13}$$

The homing rotation to be applied R_H is:

$$R_H = \psi_H - \psi_{ROBOT,N} \tag{S14}$$

The foraging trajectory is processed as follows: the experiment starts with the first orientation acquisition ψ_{INIT}. The trajectory is divided into N checkpoints C_i reached by applying a turning motion R_i, then walking straight forward. Lastly, the path integration variables are updated to obtain the departure point.

The homing procedure is divided into N_H checkpoints separated by equal distances. At each checkpoint $C_i, i \in [N+1..N+N_H]$, the robot measures its new orientation ψ_{ROBOTi} and computes its new homing angle $\psi_{H,i}$ by updating its current location (X_i, Y_i). If the difference between those two angles is greater than one average turning stride, then the robot applies the corresponding angular correction. Otherwise, the robot proceeds directly to the walking phase. This procedure results in a new position $C_{END} = C_{N+N_H} = (X_{N+N_H}, Y_{N+N_H})$.

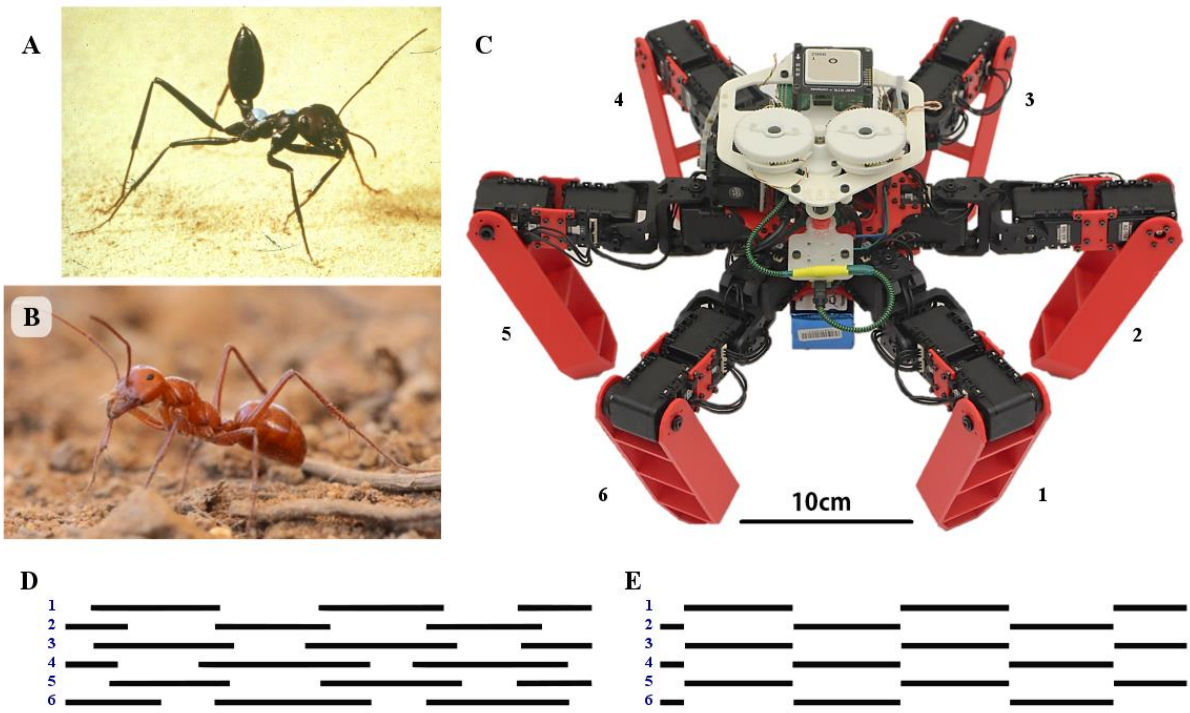

Fig. S1. AntBot, an ant-inspired hexapod robot. (A) Photograph of a North African desert ant *Cataglyphis bicolor*. From (*20*) (reprinted by permission from Springer Nature). **(B)** Photograph of an Australian desert ant *Melophorus bagoti* (courtesy of Antoine Wystrach and Sebastian Schwarz). **(C)** Photograph of the hexapod walking robot AntBot inspired by ants. **(D)-(E)** Chronographs describing the walking pattern. White bars indicate the transfer phase and black ones indicate the support phase. Numbers 1, 2 and 3 refer to the left front-, mid- and hindlegs, and numbers 6, 5 and 4, to the right front-, mid and hindlegs. **(D)** Tripod gait pattern in *Cataglyphis bicolor* desert ants at a mean speed of 60mm/s. Adapted from (*62*). **(E)** Tripod gait pattern observed in AntBot. To walk straight forward, the joints angles from the first articulations of the left legs are equal to the opposite of the ones from the right legs. When turning, all joints angles from the first articulations of each leg are equal. Tripod gait is applied both when walking straight forward or when turning.

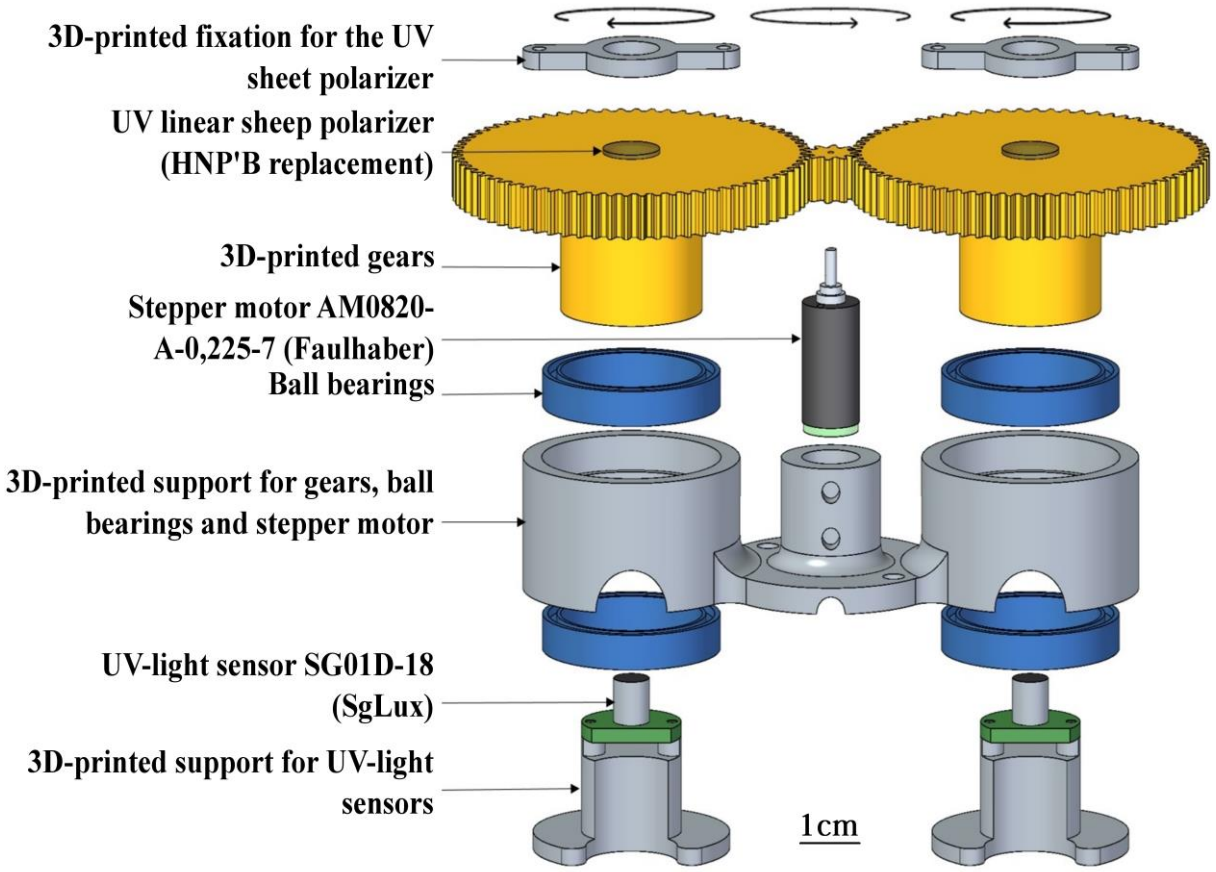

Fig. S2. Exploded computer-aided design view of the UV-polarized light compass. This diagram shows the components of the 2-pixel celestial compass. The 3-D parts can be obtained at: https://github.com/JuSquare/AntBot/tree/master/CelestialCompass.

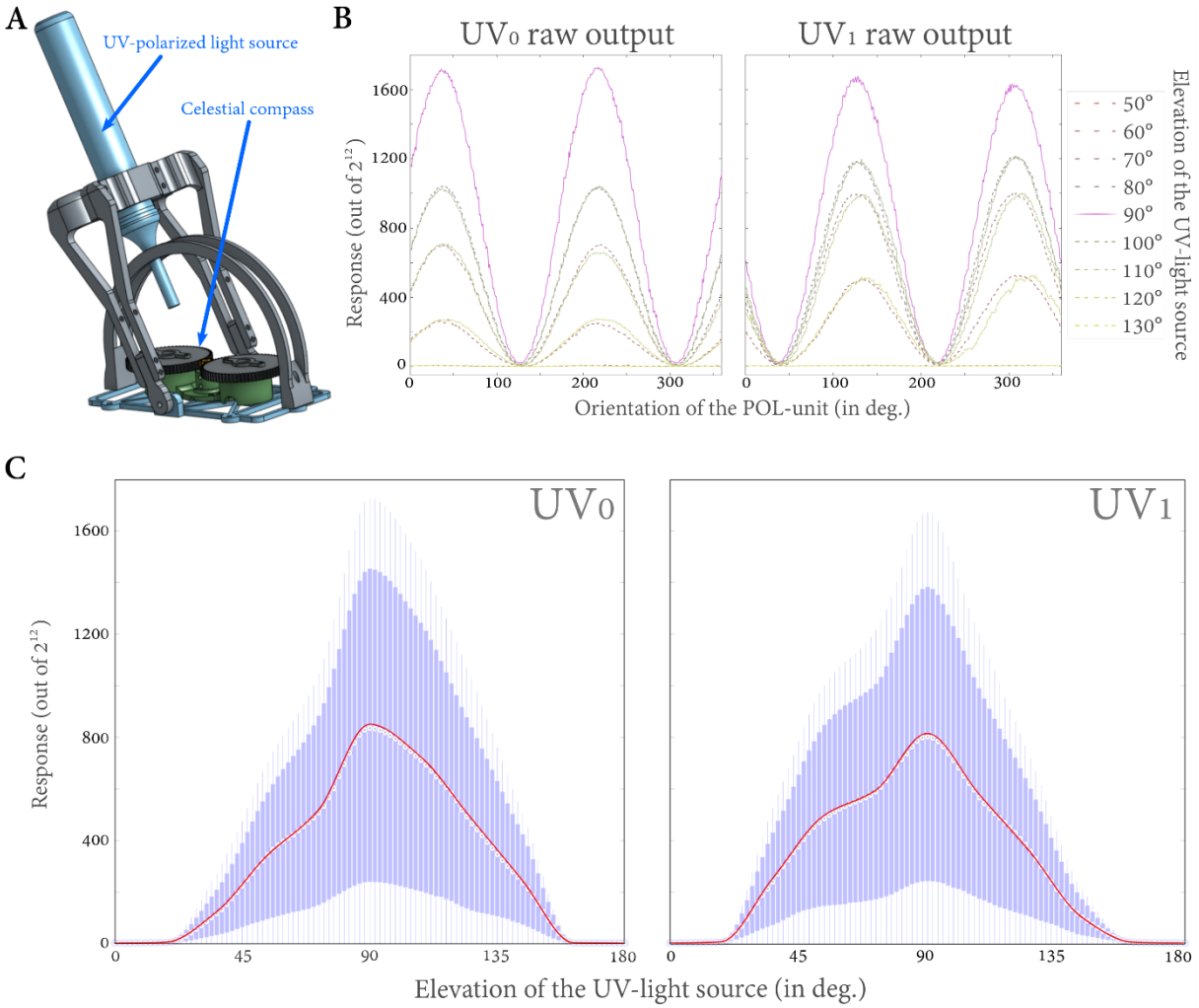

Fig. S3. Characterization of the angular aperture of the celestial compass. (A) Setup used for data acquisition with respect to the UV-polarized light source elevation. **(B)** *UV₀* (left) and *UV₁* (right) raw outputs at specific light source elevations (Polytec UV LC-5, 200mW, 365nm). The direction of polarization used in these tests was equal to 35° with respect to the mechanical support of the celestial compass. **(C)** Distribution of the maximum responses detected in *UV₀* (left) and *UV₁* (right) POL-units at light source elevations ranging from 0° to 180° by rotating the source in elevation in angular steps of 5°. The field of view of both POL-units was equal to ±60° centered at 90°.

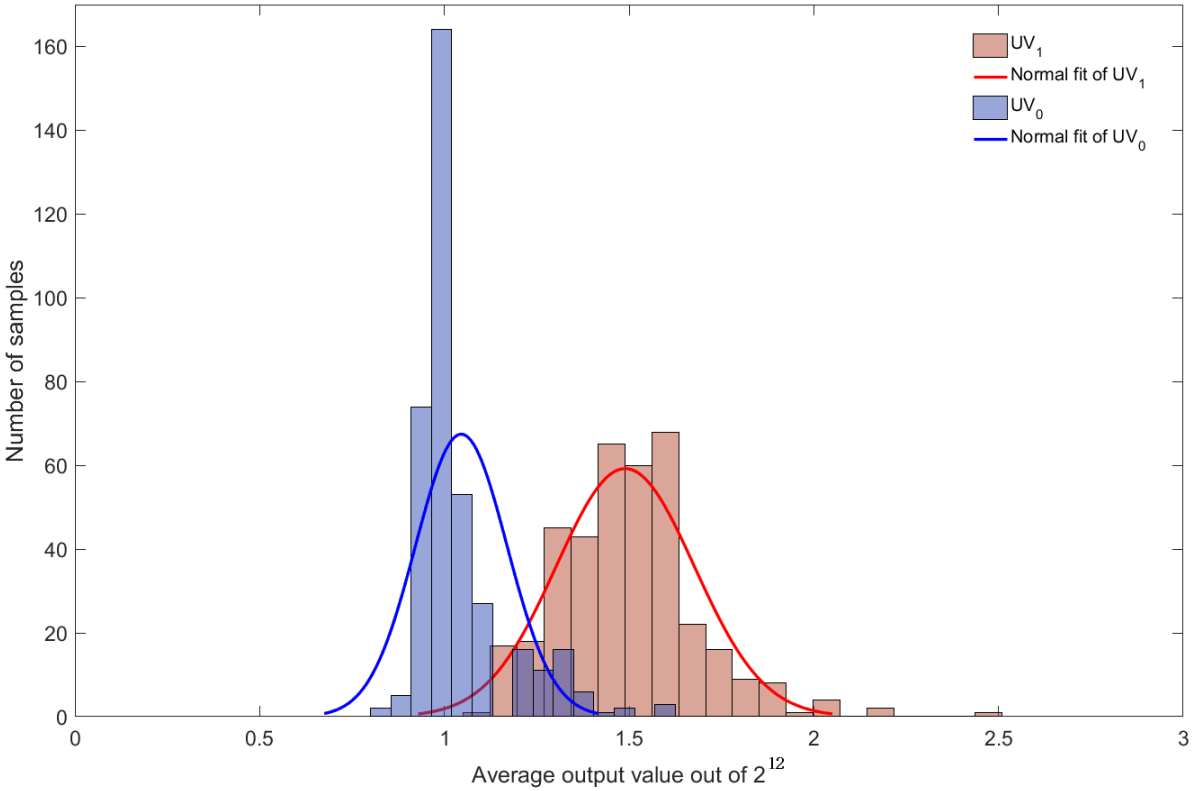

Fig. S4. Noise measured in each POL-unit in the absence of UV-polarized light. Data were acquired continuously in a UV-free environment. The POL-units' measurements showed a normal distribution (using the '*histfit*' function in Matlab) and the following characteristics: $UV_0 \sim \mathcal{N}(\mu_0 = 1.05, \sigma_0 = 0.12)$ and $UV_1 \sim \mathcal{N}(\mu_1 = 1.49, \sigma_1 = 0.19)$, $N = 6080$ samples, precision of the analog-to-digital converter equal to 12 bits. The standard deviation recorded with both POL-units was below one LSB (Least Significant Bit).

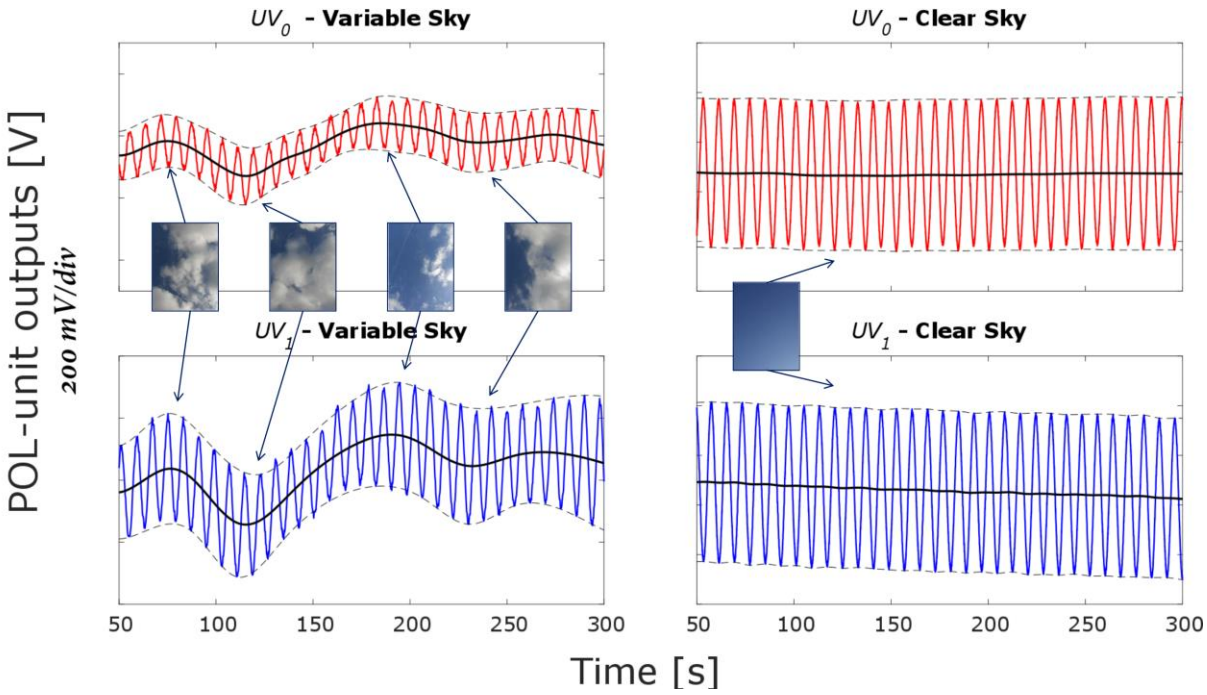

Fig. S5. Effects of variable sky on the output of the celestial compass. The continuous responses of UV_0 (red) and UV_1 (blue) POL-units (polarization units) were acquired for 5 minutes under both clear (right) and variable (left) sky conditions. The black lines give the mean UV-polarized light intensity. Under clear sky conditions, the mean intensity remained constant, apart from a slight decrease due to the solar course. Under variable sky conditions, the average light intensity oscillated due to the clouds passing over the celestial compass. These data were acquired in April 2017 in front of our laboratory, with a UV-index equal to 7 and a strong wind (65km/h according to the French Meteorological Services).

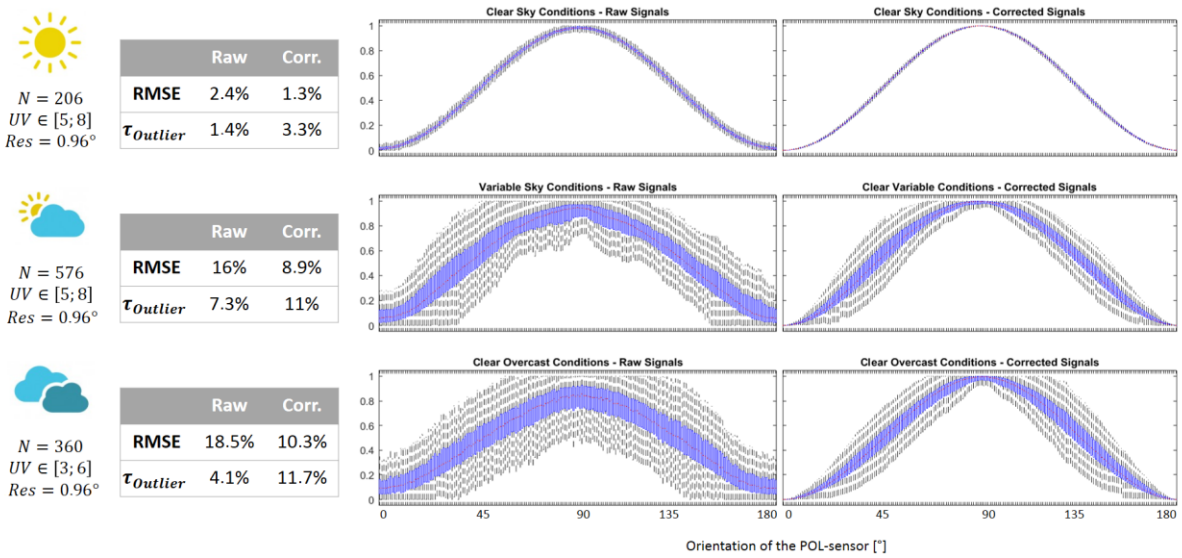

Fig. S6. Characterization of the celestial compass. The UV_0 and UV_1 POL-units' responses within [0,180°] were collected and normalized. Distributions at each orientation of the polarized filter are shown, and the mean responses are indicated by red lines. The root-mean-square error (RMSE) is given as a percentage of the overall number of points collected. The percentage of outliers detected is also specified. Results are compared between clear (top), variable (middle) and overcast (bottom) sky conditions. Mean UV-indexes are given under clear sky conditions.

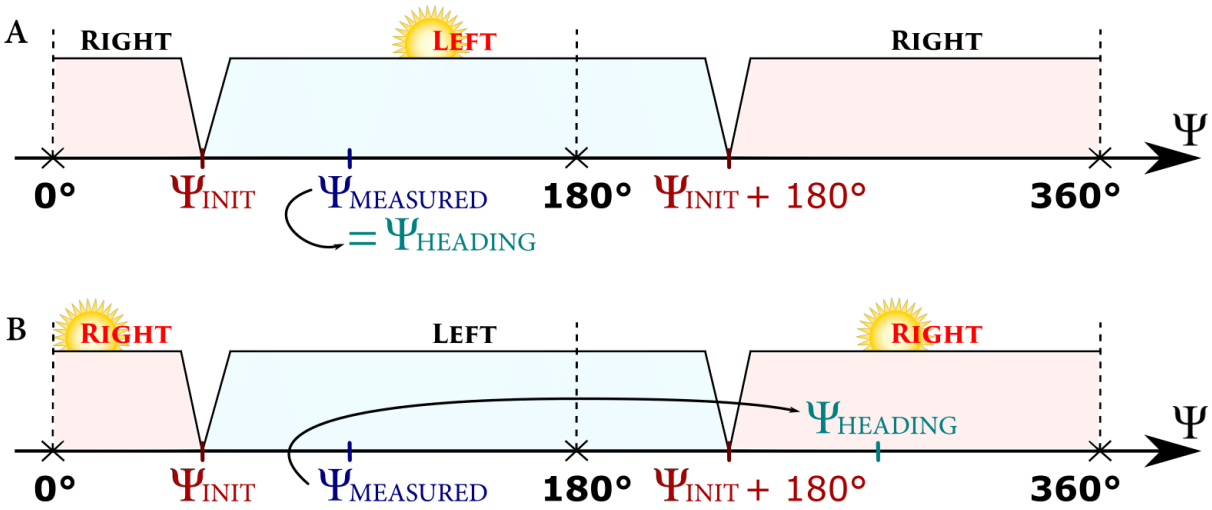

Fig. S7. Solar-based solution to the heading angle ambiguity. At the beginning of its trip, AntBot was aligned with the sun. It computed its heading angle Ψ_{INIT}, which was always set between 0° and 180°. The left and the right sides of AntBot are then defined based on Ψ_{INIT}. **(A)** When the robot has acquired a new heading angle $\Psi_{MEASURED}$, it rolls its head left and right to detect the position of the sun (corresponding to the highest UV response of the celestial compass). In this case, the heading angle measured, and the position of the sun are consistent: $\Psi_{HEADING} = \Psi_{MEASURED}$. **(B)** Here the sun was detected on the opposite side, and the heading angle measured was therefore corrected and hence, $\Psi_{HEADING} = \Psi_{MEASURED} + 180°$.

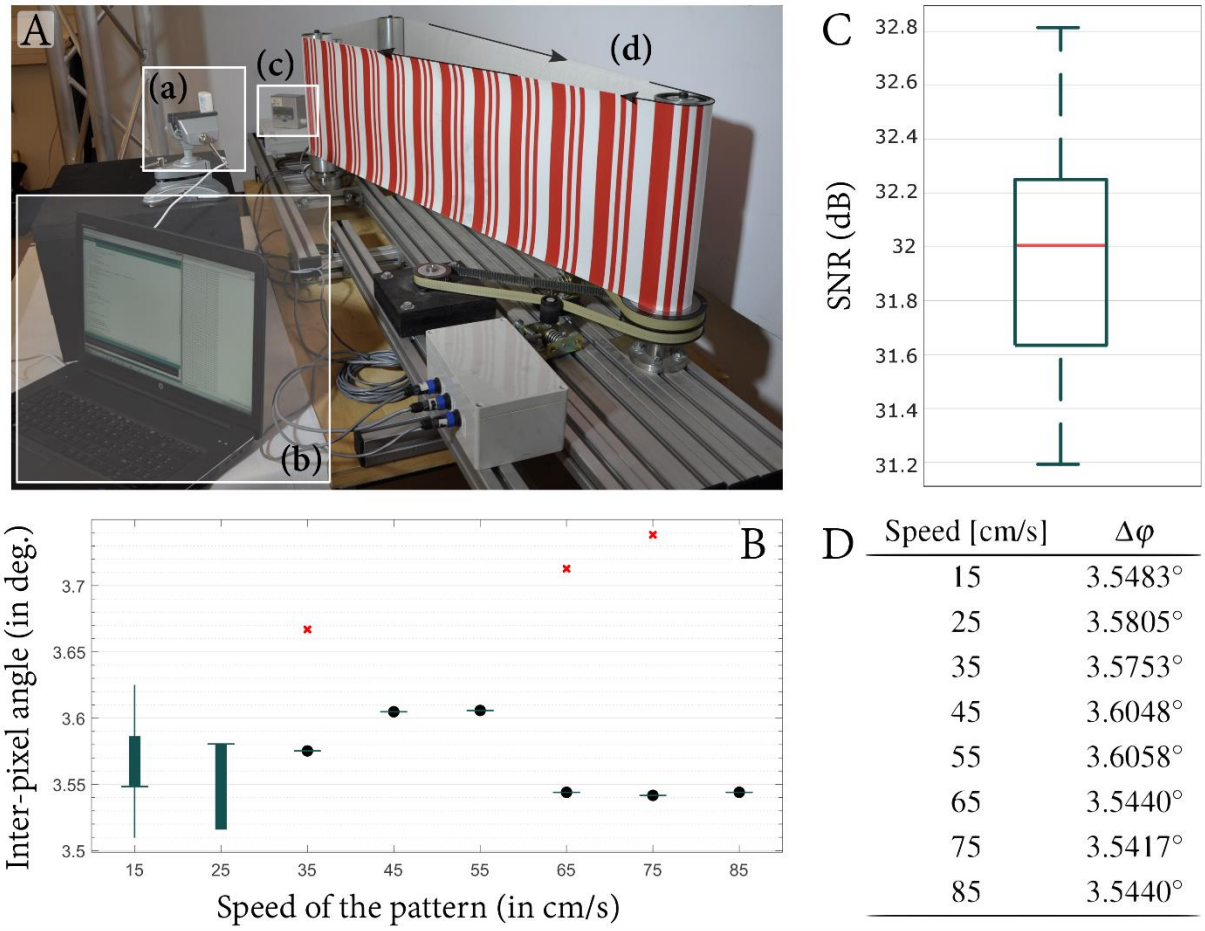

D

Speed [cm/s]	$\Delta\varphi$
15	3.5483°
25	3.5805°
35	3.5753°
45	3.6048°
55	3.6058°
65	3.5440°
75	3.5417°
85	3.5440°

Fig. S8. Characterization of the M²APix optic flow sensor. The benchmark setup is shown in **(A)** where: (a) is the M²APix sensor oriented toward a moving pattern (d) consisting of parallel red stripes. The speed of the pattern was measured with a tachometer (c). Data were collected on a laptop (b). **(B)** Boxplot of the inter-pixel angle measured at pattern speeds ranging from 15cm/s to 85cm/s. The mean value based on all the experiments, which was used in the optic flow calculations on-board AntBot was equal to 3.57°, with a low standard deviation (0.027°). **(C)** Boxplot of the SNR values. **(D)** Mean values of the inter-pixel angle. The mean signal-to-noise ratio (SNR) value was equal to 31.97dB, with a standard variation of 0.44dB. The SNR was taken to be the inverse of the sensor's coefficient of variation.

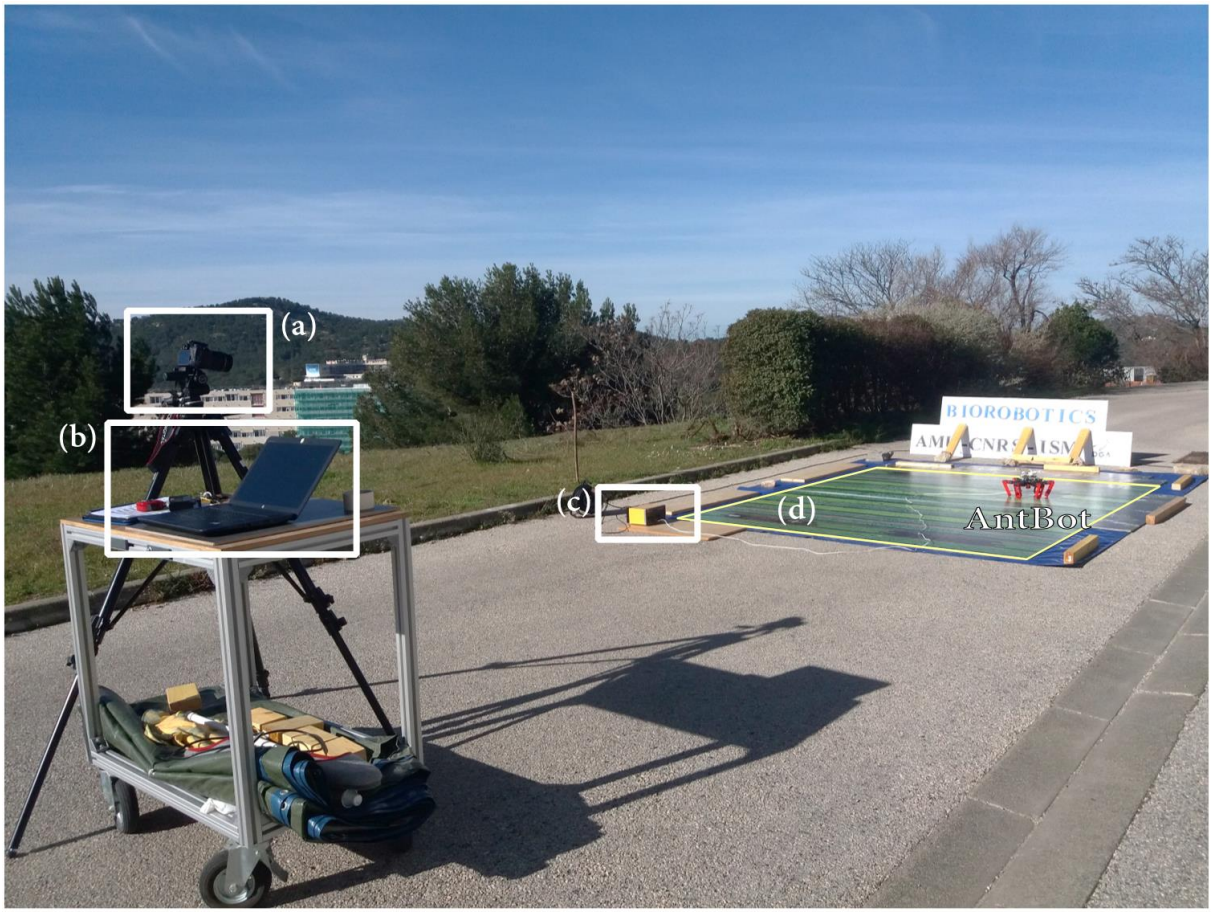

Fig. S9. Photograph of the experimental setup. AntBot navigates on a textured panel measuring 3m x 4m (d), powered by the DC generator (14V, 10A) shown in (c). The ground-truth was acquired using the high-resolution reflex camera (Canon EOS 650D) presented in (a). The experiments were managed with the host computer (b).

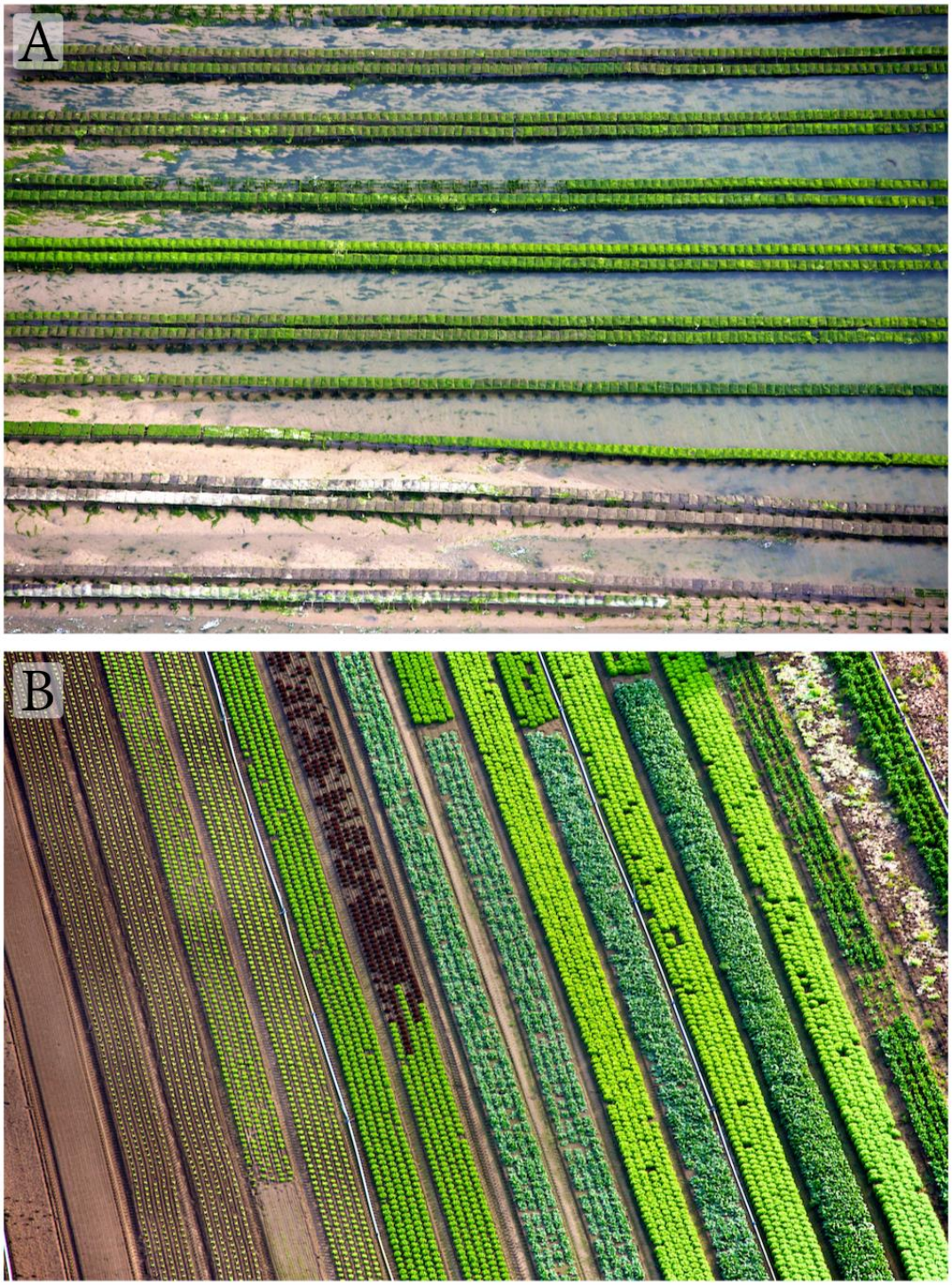

Fig. S10. Photographs of the textured panels. Sky views of an oyster farm (A) and of vegetable crops (B). These flat panels allow to quantitatively compare the five navigation modes (same textures for optic flow measurement purposes, and same slippering effects). Each panel is 3m-long and 2m-large.

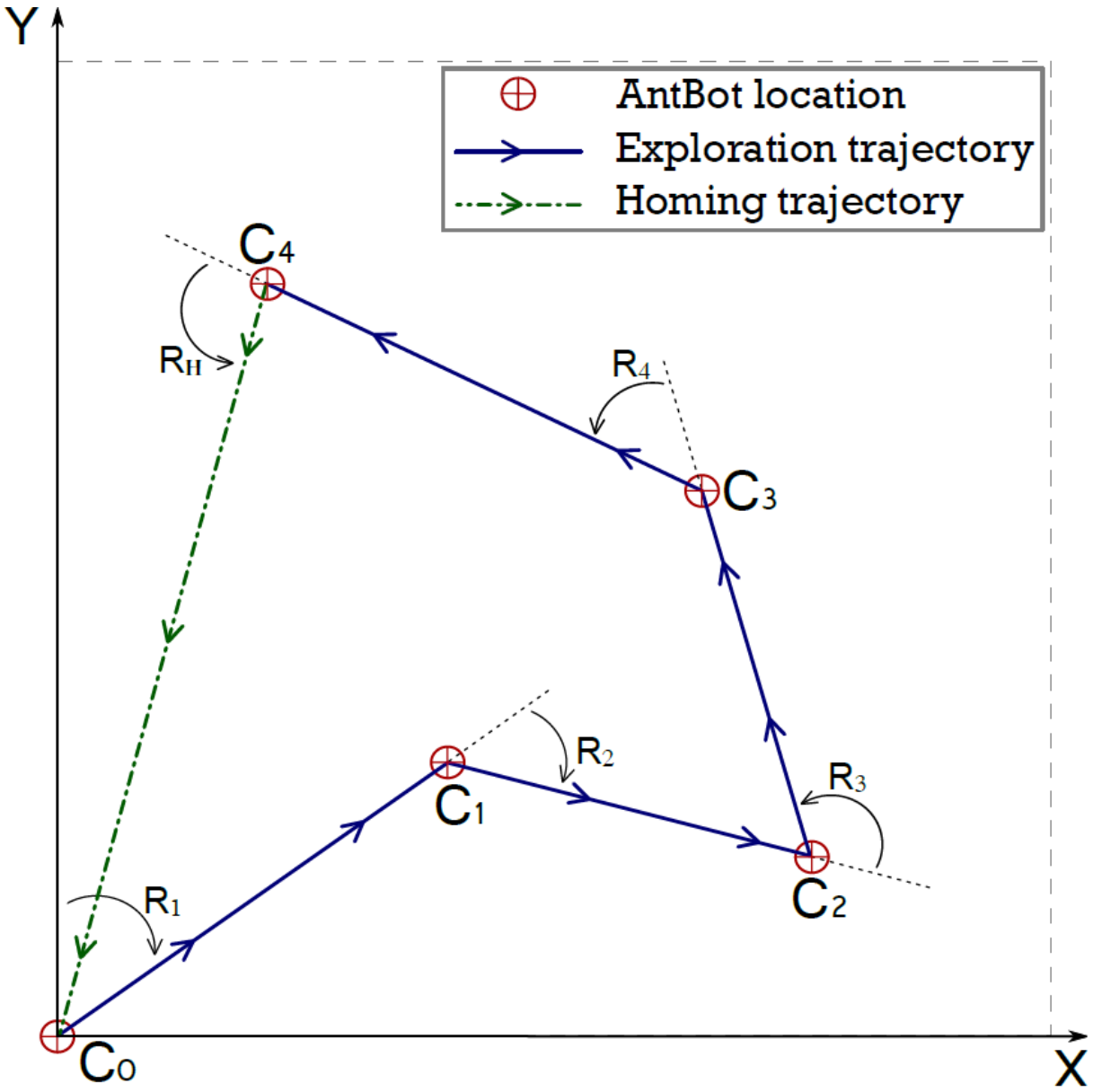

Fig. S11. Graph of the homing path. Given an exploratory trajectory including 4 checkpoints (in blue), the robot was expected to compute the homing path displayed in green taking it back to its departure point C_0. Each checkpoint C_i was reached from checkpoint C_{i-1} by applying a turning motion R_i and then walking straight forward until a pre-programmed number of steps was reached.

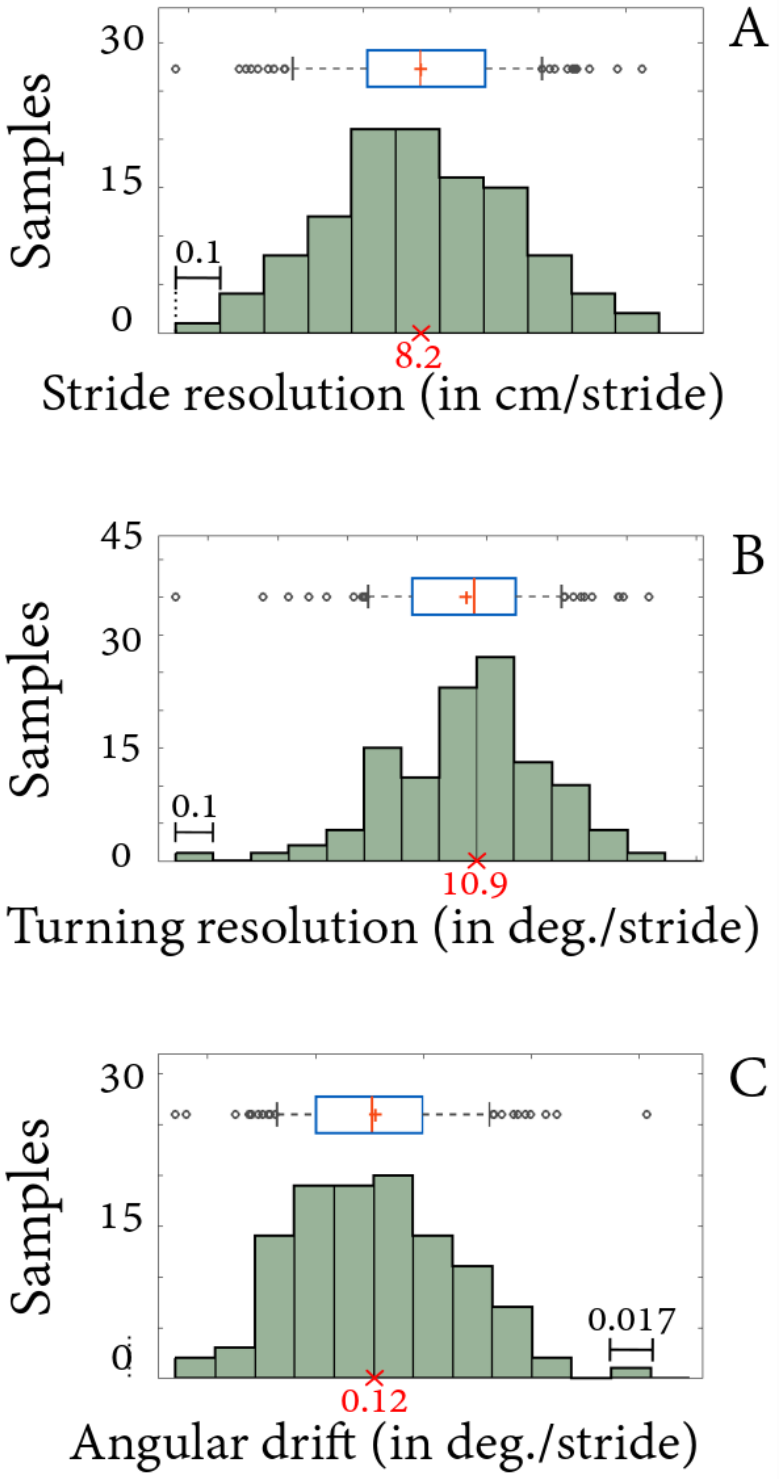

Fig. S12. AntBot's walking drift analysis. **(A)** Stride resolution of AntBot using the following experimental parameters: mean stride length, 8.2cm/stride, which is not different from a normal distribution (Lilliefors normality test, p-value = 0.500, n = 112 samples). **(B)** Turning resolution of AntBot with the same walking parameters. Mean turning angle: 10.9°/stride with a normal distribution (Lilliefors normality test, p-value = 0.394, n = 112 samples). **(C)** AntBot's angular drift per straight forward walking stride. Mean angular drift: 0.12°/stride with an almost normal distribution (Lilliefors normality test, p-value = 0.425, n = 112 samples).

Parameter	Description	Minimum	Maximum	AntBot's values
FREQ	Frequency of the walking strides performed	0.2Hz	3Hz	1.0Hz
DX	Amplitude of a straight forward stride length	10	75	30 (~8.2cm/stride)
DY	Amplitude of a straight sideward stride length	10	75	0
TURN	Amplitude of a turning stride length	5.1	10	5.5 (~10.9°/stride)
ALT	Height of the legs' end while being transferred	10mm	50mm	20mm

Table S1. Walking parameters of the hexapod robot AntBot. According to these parameters, the robot's walking speed during the experiments was approximately equal to 10cm/s, with a mean stride length of 8.2cm and a mean turning angle per turning stride of 10.9°.

Number of strides	Morning	Afternoon
1 or 2	0.667	0.500
3	0.850	0.750
More than 3	0.980	0.980

Table S2. Empiric gain β used for the outdoor experiments.

Day and time	UV	Weather	G.T. Homing error	Robot's Homing error	G.T. Homing distance	Robot's Homing distance	Homing Success
First 20 experiments (on the same trajectory)							
01/05	-	-	27.7	0.1	176.8	190.2	No
01/05	-	-	38.1	0.1	208.5	190.2	No
01/05	-	-	26.5	0.1	196.4	190.2	No
01/05	-	-	42.2	0.1	202.4	190.2	No
01/05	-	-	44.5	0.1	204.9	190.2	No
01/05	-	-	51.7	0.1	174.5	190.2	No
01/05	-	-	40.1	0.1	182.8	190.2	No
01/05	-	-	41.1	0.1	189.5	190.2	No
01/05	-	-	53.8	0.1	192.8	190.2	No
01/05	-	-	58.5	0.1	176.5	190.2	No
01/06	-	-	68.0	0.1	162.3	190.2	No
01/06	-	-	51.4	0.1	171.8	190.2	No
01/06	-	-	51.3	0.1	174.8	190.2	No
01/06	-	-	48.4	0.1	177.7	190.2	No
01/06	-	-	51.2	0.1	178.5	190.2	No
01/06	-	-	55.6	0.1	166.9	190.2	No
01/06	-	-	65.7	0.1	156.7	190.2	No
01/06	-	-	44.2	0.1	160.1	190.2	No
01/06	-	-	48.8	0.1	171.8	190.2	No
01/06	-	-	51.8	0.1	169.5	190.2	No
5 random trajectories							
01/20	-	-	73.6	4.0	283.5	260.1	No
01/20	-	-	37.9	5.6	101.9	93.6	No
01/20	-	-	132.0	4.5	450.4	446.8	No
01/20	-	-	108.2	2.3	272.5	256.4	No
01/20	-	-	27.8	5.3	44.0	29.8	No
10-checkpoint trajectory							
02/15	-	-	171.1	4.2	265.2	234.3	No
Results							
Homing error: RMSE robot vs. G.T.			**Homing distance: RMSE robot vs. G.T.**			**Homing success rate**	
65.0cm			**18.0cm**			**0%**	

Table S3. Results obtained in the PI-ST mode. This homing mode was tested by estimating the robot's heading angle and the distance travelled by integrating the strides. The homing performances are listed here in terms of the homing distance (*i.e.* the length of the homeward trajectory), the homing error, and the homing success. Distances are given in cm. The ground truth (G.T.) was given by our 17-motion cameras system. The robot's belief is given for the sake of comparison. To be counted as a success, the homing error had to be less than 22.5cm, which is half of the robot's height. The root means square error (RMSE) of both the homing error and homing distance between the ground truth and the robot's belief is presented at the bottom of the figure.

Day and time	UV	Weather	G.T. Homing error	Robot's Homing error	G.T. Homing distance	Robot's Homing distance	Homing Success
First 20 experiments (on the same trajectory)							
01/07	-	-	41,1	6.2	211,9	217.0	No
01/07	-	-	38,7	1.0	194,3	192.6	No
01/07	-	-	30,4	5.3	181,8	196.1	No
01/07	-	-	38,8	3.2	198,4	183.2	No
01/07	-	-	39,9	8.2	201,3	205.7	No
01/07	-	-	13,9	1.9	192,6	207.6	Yes
01/07	-	-	22,3	2.0	192,8	206.8	Yes
01/07	-	-	32,4	6.9	185,6	202.2	No
01/07	-	-	29,0	1.8	187,8	210.8	No
01/07	-	-	44,8	3.9	201,6	184.1	No
01/08	-	-	49,3	2.5	205,1	188.2	No
01/08	-	-	34,4	6.9	204,5	203.8	No
01/08	-	-	14,6	7.8	195,2	229.3	Yes
01/08	-	-	28,8	5.1	198,7	200.3	No
01/08	-	-	3,4	1.9	186,4	184.2	Yes
01/08	-	-	39,9	2.9	204,8	192.7	No
01/08	-	-	46,3	4.8	205,0	184.3	No
01/08	-	-	18,3	6.7	188,3	198.4	Yes
01/08	-	-	40,9	3.1	176,6	195.0	No
01/08	-	-	34,6	2.8	183,7	195.7	No
5 random trajectories							
01/20	-	-	63,8	2.9	265,0	237.6	No
01/20	-	-	65,1	7.3	130,6	113.2	No
01/20	-	-	156,5	4.8	438,7	428.8	No
01/20	-	-	116,5	2.4	274,0	239.6	No
01/20	-	-	19,5	1.0	42,1	35.7	Yes
10-checkpoint trajectory							
02/15	-	-	18.9	6.8	218.5	232.4	Yes
Results							
Homing error: RMSE robot vs. G.T.			**Homing distance: RMSE robot vs. G.T.**			**Homing success rate**	
48.8cm			**16.6cm**			**26.9%**	

Table S4. Results obtained in the PI-OF-ST mode. This homing mode was tested by estimating the robot's heading angle by integrating the strides and the distance travelled, by integrating the ventral optic flow. The homing performances are listed here in terms of the homing distance (*i.e.* the length of the homeward trajectory), the homing error, and the homing success. Distances are given in cm. The ground truth (G.T.) was obtained by our 17-motion cameras system. The robot's belief is given for the sake of comparison. To be counted as a success, the homing error had to be less than 22.5cm, which is half of the robot's height. The root means square error (RMSE) of both the homing error and the homing distance between the ground truth and the robot's belief is presented at the bottom of the figure.

Day and time	UV	Weather	G.T. Homing error	Robot's Homing error	G.T. Homing distance	Robot's Homing distance	Homing Success
First 20 experiments (on the same trajectory)							
01/09	-	-	47,3	2.6	201,2	183.6	No
01/09	-	-	36,7	3.9	198,0	191.3	No
01/09	-	-	33,9	3.9	208,3	198.0	No
01/09	-	-	33,3	4.9	197,1	197.4	No
01/09	-	-	30,0	5.0	184,6	192.2	No
01/09	-	-	39,5	5.5	205,0	191.8	No
01/09	-	-	44,0	5.0	208,1	198.1	No
01/09	-	-	31,0	6.4	203,6	204.4	No
01/09	-	-	43,0	5.9	192,3	190.2	No
01/09	-	-	31,1	8.1	189,2	194.8	No
01/10	-	-	47,7	2.5	196,3	182.8	No
01/10	-	-	21,6	5.6	178,2	187.4	Yes
01/10	-	-	37,4	2.2	201,7	194.8	No
01/10	-	-	48,7	4.7	201,6	183.4	No
01/10	-	-	46,6	7.4	203,6	188.1	No
01/10	-	-	44,2	7.9	196,0	196.4	No
01/10	-	-	44,0	7.4	190,1	201.3	No
01/10	-	-	49,5	7.5	192,9	188.1	No
01/10	-	-	29,1	2.9	173,0	196.3	No
01/10	-	-	41,9	5.4	181,8	193.4	No
5 random trajectories							
01/20	-	-	53,8	2.9	260,4	270.0	No
01/20	-	-	27,3	2.4	91,3	94.4	No
01/20	-	-	148,0	4.2	440,3	456.0	No
01/20	-	-	132,2	7.7	277,1	265.1	No
01/20	-	-	10,2	3.5	38,5	35.4	Yes
10-checkpoint trajectory							
02/15	-	-	46.4	2.8	240.1	227.4	No
Results							
Homing error: RMSE robot vs. G.T.			**Homing distance: RMSE robot vs. G.T.**			**Homing success rate**	
50.1cm			**11.1cm**			**7.7%**	

Table S5. Results obtained in the PI-ST-FUSE mode. This homing mode was tested by estimating the robot's heading angle by integrating the strides and the travel distance by integrating both the strides and the ventral optic flow. The homing performances are listed here in terms of the homing distance (*i.e.* the length of the homeward trajectory), the homing error, and the homing success. Distances are given in cm. The ground truth (G.T.) was obtained by our 17-motion cameras system. The robot's belief is given for the sake of comparison. To be counted as a success, the homing error had to be less than 22.5cm, which is of half of the robot's height. The root means square error (RMSE) of both the homing error and the homing distance between the ground truth and the robot's belief is presented at the bottom of the figure.

Day and time	UV	Weather	G.T. Homing error	Robot's Homing error	G.T. Homing distance	Robot's Homing distance	Homing Success
First 20 experiments (on the same trajectory)							
01/12 9:45am	1.0	Clear	14,7	7.9	177,7	150.8	Yes
01/12 10:10am	1.0	Clear	7,6	6.5	171,4	167.6	Yes
01/12 10:35am	1.0	Clear	27,2	2.8	163,3	172.9	No
01/17 11:00am	1.3	Clear	17,7	7.1	160,9	153.4	Yes
01/17 11:35am	1.3	Clear	31,9	0.6	151,8	139.1	No
01/17 11:55am	1.3	Clear	23,1	2.1	131,7	160.7	No
01/11 2:00pm	1.0	Clear	28,8	4.5	173,2	154.2	No
01/18 9:15am	1.4	Clear	17,5	2.8	164,2	148.4	Yes
01/18 9:40am	1.4	Clear	8,8	2.7	164,2	156.3	Yes
01/18 10:05am	1.4	Clear	18,2	4.4	153,6	142.4	Yes
01/18 10:25am	1.4	Clear	27,6	2.8	144,7	132.6	No
01/18 11:00am	1.4	Clear	19,8	3.9	155,5	149.9	Yes
01/18 1:50pm	1.4	Clear	11,9	4.9	158,7	159.6	Yes
01/18 2:35pm	1.4	Clear	16,6	6.3	155,0	148.6	Yes
01/18 2:55pm	1.4	Clear	15,2	5.0	147,5	142.9	Yes
01/18 3:15pm	1.4	Clear	21,7	7.7	154,8	144.7	Yes
01/18 3:35pm	1.4	Clear	24,0	5.2	160,6	149.6	No
01/18 3:50pm	1.4	Clear	26,5	3.9	141,3	133.7	No
01/18 4:10pm	1.4	Clear	25,0	7.1	160,6	149.1	No
01/19 2:05pm	1.4	Clear	12,8	0.7	167,6	160.9	Yes
5 random trajectories							
02/09 2:15pm	1.6	Clear	19,2	2.7	291,3	271.5	Yes
02/09 2:45pm	1.6	Clear	30,9	7.9	139,7	125.1	No
02/09 3:10pm	1.6	Clear	13,7	1.8	413,5	434.0	Yes
02/09 3:35pm	1.6	Clear	33,7	3.6	299,0	268.8	No
02/13 2:30pm	1.5	Cloudy	20,6	3.8	99,6	92.7	Yes
10-checkpoint trajectory							
02/14 10:35am	1.5	Clear	53.6	1.6	322.8	296.8	No
Results							
Homing error: RMSE robot vs. G.T.			**Homing distance: RMSE robot vs. G.T.**			**Homing success rate**	
20.3cm			**15.3cm**			**57.7%**	

Table S6. Results obtained in the PI-POL-ST mode. This homing mode was tested by estimating the robot's heading angle using the celestial compass and the travel distance, by integrating the strides. The homing performances are listed here in terms of the homing distance (*i.e.* the length of the homeward trajectory), the homing error, and the homing success. Distances are given in cm. The ground truth (G.T.) was based on photographs. The robot's belief is given for the sake of comparison. As the experiments were conducted outdoors, the environmental and meteorological conditions are specified. To be counted as a success, the homing error had to be less than 22.5cm which is half of the robot's height. The root means square error (RMSE) of both the homing error and the homing distance between the ground truth and the robot's belief is given at the bottom of the figure.

Day and time	UV	Weather	G.T. Homing error	Robot's Homing error	G.T. Homing distance	Robot's Homing distance	Homing Success
First 20 experiments (on the same trajectory)							
01/31 11:40am	1.6	Clear – 8300Lux	12,2	3.0	168,4	162.3	Yes
01/31 12:00am	1.6	Clear – 8700Lux	7,4	1.4	157,9	148.8	Yes
02/07 9:50am	1.5	Clear – 7100Lux	4,9	1.7	185,5	167.8	Yes
02/04 4:00pm	1.5	Clear – 9000Lux	8,0	2.6	141,0	139.1	Yes
01/22 2:50pm	1.4	Cloudy – 6500Lux	10,1	5.7	166,0	159.8	Yes
02/07 10:15am	1.5	Clear – 8000Lux	2,5	7.1	121,9	123.2	Yes
02/07 2:00pm	1.5	Clear – 147000Lux	4,7	5.3	186,6	171.5	Yes
01/23 2:30pm	1.3	Clear – 9450Lux	10,6	1.6	181,8	190.3	Yes
02/07 14:55pm	1.5	Clear – 127000Lux	5,3	6.8	187,4	183.3	Yes
01/23 3:15pm	1.3	Clear – 8050Lux	9,6	5.1	176,4	182.6	Yes
02/08 13:30pm	1.5	Clear – 135000Lux	6,4	7.2	167,2	175.0	Yes
01/23 3:55pm	1.3	Clear – 6100Lux	5,5	7.0	183,1	188.0	Yes
02/08 3:00pm	1.5	Clear – 116000Lux	4,6	2.9	160,6	139.1	Yes
01/24 3:05pm	1.4	Cloudy – 8000Lux	7,7	2.4	146,2	155.9	Yes
01/24 3:35pm	1.4	Cloudy – 5500Lux	8,9	4.5	174,0	167.1	Yes
01/28 2:40pm	1.4	Clear – 7700Lux	13,6	3.3	183,6	192.6	Yes
02/08 3:25pm	1.5	Clear – 110000Lux	6,9	3.7	176,5	163.3	Yes
01/31 10:30am	1.6	Clear – 7500Lux	3,0	4.3	172,7	171.2	Yes
01/31 11:00am	1.6	Clear – 7800Lux	1,2	7.7	173,9	167.5	Yes
01/31 11:20am	1.6	Clear – 8000Lux	7,1	5.4	172,4	165.2	Yes
5 random trajectories							
02/14 2:50pm	1.5	Cloudy – 82000Lux	4,1	6.9	303,6	311.5	Yes
02/14 3:15pm	1.5	Cloudy – 76000Lux	5,4	0.7	120,3	115.4	Yes
02/14 3:45pm	1.5	Cloudy – 23000Lux	7,8	8.0	444,0	435.6	Yes
02/16 2:55pm	1.6	Cloudy – 54000Lux	8,0	8.2	263,8	265.6	Yes
02/16 3:30pm	1.6	Cloudy – 32000Lux	1,3	2.6	46,2	42.1	Yes
10-checkpoint trajectory							
02/14 11:35am	1.5	Clear – 114500Lux	6.5	4.6	305.8	324.4	Yes
Results							
Homing error: RMSE robot vs. G.T.			**Homing distance: RMSE robot vs. G.T.**			**Homing success rate**	
4.6cm			**9.6cm**			**100%**	

Table S7. Results obtained in the PI-FULL mode. This homing mode was tested by estimating the robot's heading angle using the celestial compass and the distance travelled by integrating both the strides and the ventral optic flow. The homing performances are listed here in terms of the homing distance (*i.e.* the length of the homeward trajectory), the homing error, and the homing success. Distances are given in cm. The ground truth (G.T.) was obtained by our 17-motion cameras system. The robot's belief is given for the sake of comparison. As the experiments were conducted outdoors, the environmental and meteorological conditions are specified. To be counted as a success, the homing error had to be less than 22.5cm, which is half of the robot's height. The root means square error (RMSE) of both the homing error and the homing distance between the ground truth and the robot's belief is given at the bottom of the figure.

Supplementary Videos

Movie S1 (.mp4 format). AntBot's homing performance in the PI-ST mode
This movie presents the homing performance of the hexapod robot AntBot when its path integration mode was set to the PI-ST mode, which means that it computed both the distance travelled and its orientation on the basis of stride integration alone.

Movie S2 (.mp4 format). AntBot's homing performance in the PI-OF-ST mode
This movie presents the homing performance of the hexapod robot AntBot when its path integration mode was set to the PI-OF-ST mode, which means that the distance travelled was computed based on ventral optic flow integration, and the orientation, based on stride integration alone.

Movie S3 (.mp4 format). AntBot's homing performance in the PI-ST-FUSE mode
This movie presents the homing performance of the hexapod robot AntBot when its path integration mode was set to PI-ST-FUSE, where the optic flow cues and stride information were merged to estimate the distance travelled, and the orientation was determined based on stride integration alone.

Movie S4 (.mp4 format). AntBot's homing performance in the PI-POL-ST mode
This movie presents the homing performance of the hexapod robot AntBot when its path integration mode was set to PI-POL-ST, which means that its travel distance was calculated based on stride integration and its orientation was determined using the celestial compass.

Movie S5 (.mp4 format). AntBot's homing performance in the PI-FULL mode
This movie presents the homing performance of the hexapod robot AntBot when its path integration mode was set to PI-FULL. In the case of this fully ant-inspired mode, the distance travelled was computed based on both stride integration and optic flow cues, and the orientation was determined using the celestial compass.

Supplementary Data

The trajectories of the hexapod robot AntBot in the 130 tests performed can be found at:

https://github.com/JuSquare/AntBot/tree/master/Experiments

The 3D parts of the celestial compass can be found at:

https://github.com/JuSquare/AntBot/tree/master/CelestialCompass

The 3D parts of the robot AntBot can be found at:

https://github.com/JuSquare/AntBot/tree/master/3D Parts